THE SIGNIFICANCE OF CONVECTIVE CLOUD MICROPHYSICS FOR CLIMATE MODEL SIMULATIONS OF RAINFALL IN THE WEST AFRICAN SAHEL AT SEASONAL TIME SCALES

by

LYNNE C. TRABACHINO

A dissertation submitted to the

Graduate School – New Brunswick

Rutgers, The State University of New Jersey

In partial fulfillment of the requirements

For the degree of

Doctor of Philosophy

Graduate Program in Atmospheric Science

Written under the direction of

Mark A. Miller

And approved by

_____

_____

_____

_____

_____

New Brunswick, New Jersey

October, 2016

ABSTRACT OF THE DISSERTATION

The Significance of Convective Cloud Microphysics for Climate Model Simulations of Rainfall in the West African Sahel at Seasonal Time Scales

by LYNNE C. TRABACHINO

Dissertation Director:

Mark A. Miller

This study uses a non-traditional method to substantiate the underlying influence of the parameterization of subgrid-scale convective processes on the capability of the latest generation of global climate models to simulate the seasonal cycle of rainfall associated with the West African monsoon and establish a direct connection between the treatment of convective rainfall and overall model performance on seasonal time scales. To establish the degree to which convective parameterizations

may influence model simulations at seasonal scales more definitively, a single column of grid-scale output was extract from an emissions scenario experiment for two coupled models and compared to the observed evolution of rainfall, surface meteorology, the thermodynamic state of the atmosphere, clouds and radiation, obtained during 2006 in Niamey, Niger. Overall both models demonstrated a remarkable capability to comprehensively capture the seasonal cycle of the West African monsoon in the vicinity of Niamey. However, the results confirm that deficiencies in subgrid-scale physics can be a significant source of error with regards to the timing of simulated rainfall at seasonal scales and, in some models dominate non-local sources of error. Comparison of the performance of each model and their respective convective parameterizations indicated that the capability to simulate the seasonal cycle of rainfall in the Sahel with realistic timing appears to be more sensitive to a realistic representation of convective precipitation microphysics than to a realistic representation of the organization of convective structures. The perspective gained from this study sheds a more positive light on the present capabilities of coupled models to simulate convection in the Sahel and suggests that resolution of the long-standing disagreement in rainfall projections among

different coupled models may be more within reach than previously advocated by performance evaluations based on traditional methods.

Acknowledgements

I would first like to convey my sincere thanks to my advisor, Dr. Mark Miller, for his time and support throughout my graduate career. I am deeply appreciative for his patient guidance during the development and completion of this dissertation, and dedication to my intellectual growth as a scientist and an educator. Mark has been a great mentor and friend. Without his unwavering belief in me, I would not be where I am today. I am also very grateful to my committee members, Dr. Anthony Broccoli, Dr. Leo Donner, Dr. Anthony Del Genio, and Dr. Ben Lintner, for their indispensable feedback and encouraging response to my research goals. To have each of these individuals serve me in this capacity is truly an honor.

The completion of this dissertation would not have been possible without collaborative effort. I am especially indebted to Dr. Michael Jensen and Tami Toto of Brookhaven National Laboratory who turned the idea of merging radiometric retrievals with radiosonde measurements into a reality. I would also like to thank the past and present members of Mark Miller's physical meteorology research group at Rutgers, including Dr. Virendra Ghate, Dr. Allison Collow, Lu Wang, Zhongyu Kuang, Bryan Raney, Jenny Kafka, and Matthew Drews, for providing useful

suggestions and feedback that contributed to the development of this work, and for the opportunity to contribute to their projects as well. I would like to recognize John Kelley, my wonderful supervisor while at Lockheed Martin, who gave me a great start to my career and encouraged me to pursue graduate work.

I am deeply indebted to my family and friends for supporting me on a personal level. I would like to thank my parents, John and Carole Trabachino, for the many personal sacrifices they made so that I could continue to pursue my education. I would also like to thank my sister and her husband, Christine and Nick Minerowicz, for always opening their home to me and the countless other ways they have helped me through the last few years. Finally, I thank two very special friends, Alysun Folden and Jay Arch, for their emotional support and encouragement.

Contents

List of Tables

List of Illustrations

radiosonde observations (SONDE) while deployed as part of the Atmospheric Radiation Measurement (ARM) program's first ARM Mobile Facility (AMF1) between 2005 and 2013. Temperature profile errors are presented as (a) mean (bias) and (b) root-mean-square (RMS) discrepancies (defined as T_{mwrp} - T_{sonde}) for AMF1 deployments in Niamey, Niger (NIM, red), Shouxian, China (HFE, yellow), Black Forest, Germany (FKB, green), Cape Cod, Massachusetts (PVC, light blue), Point Reyes, California (PYE, dark blue), and Graciosa Island, Azores (GRW, purple). RMS discrepancies are compared to errors typically assigned by the National Center for Environmental Prediction (NCEP) to radiosonde observations when used in numerical weather model applications (black dashed line). Plots (c) and (d) are the same as (a) and (b), except for water vapor density in $\mathrm{g \cdot m^{-3}}$.

Fig. 3.2. Example vertical profiles of temperature in °C from the MWRP (solid lines) and SONDE (dashed lines) from (a) NIM on 07 August 2006 at 05:35 LST, (b) HFE on 26 July 2008 at 05:26 LST, (c) FKB on 23 August 2007 at 23:24 LST, (d) PVC on 25 October 2012 at 11:15 LST, (e) PYE on 10 August 2005 at 12:00 LST, and (f) GRW on 09 April 2010 at 05:29 LST.

Fig. 3.3. Same as Fig. 3.2, except for water vapor density in $\mathrm{g \cdot m^{-3}}$.

Fig. 3.4. $\mathrm{MS_{ecmwf}}$ flow chart.

Fig. 3.5. Time-height cross sections of temperature in °C for August 11, 2006 in Niamey, Niger from the (a) MS_{ecmwf} and (b) MS_{mwrp} high-resolution radiosonde-related data products, and (c) the temperature discrepancy between the two products, defined as MS_{ecmwf} - MS_{mwrp}. Plots (d) - (f) are the same as (a) - (c), except for relative humidity in %. MS_{ecmwf} was generated by combining radiosonde observations with ECMWF model output. MS_{mwrp} was generated using an identical algorithm, except that vertical profiles of temperature derived from the AMF1 MWRP were used in place of model output.

Fig. 3.6. Bias (solid lines) and RMS error (dashed lines) in MS_{ecmwf} profiles of (a) temperature in °C, (b) water vapor density in g/m^3, and (c) relative humidity in % for the six-month period of May through October of 2006 in Niamey, Niger.

Fig. 3.7. Comparison of (a) diurnal and (b) seasonal cycles of CAPE (solid lines) and CIN (dashed lines) in kJ/kg derived from MS_{ecmwf} (red lines) and MS_{mwrp} (black lines) for the six-month period including May through October of 2006.

Fig. 3.8. Temperature dependencies of (a) ice water content in g/m^3, (b) liquid water content in g/m^3, (c) ice cloud particle effective radius in μm, and (d) liquid cloud droplet effective radius in μm as defined in the MICROBASE VAP algorithm assuming a total radar reflectivity factor of -10 dBZ. Error bars represent the

variability resulting from a 3 °C (red) and 1 °C (black) uncertainty in input temperature profiles.

Fig. 4.1 Time series of monthly-mean (a) accumulated rainfall, (b) near-surface air temperature, (c) near-surface dew point temperature, (d) near-surface wind speed and (e) wind direction, (f) surface barometric pressure, (g) near-surface moist static energy, (h) lifted condensation level (LCL), (i) convective available potential energy (CAPE), (j) convective inhibition (CIN), (k) cloud area fraction, (l) liquid water path (LWP), (m) integrated water vapor, (n) surface latent heat flux, (o) surface sensible heat flux, (p) surface downwelling shortwave (SW) radiation, (q) surface downwelling SW radiation for clear sky conditions, (r) surface downwelling longwave (LW) radiation, (s) surface downwelling LW radiation for clear sky conditions, and (t) surface upwelling LW radiation derived from AMF-1 measurements at the Niamey Airport site during 2006. Months included in the 2006 wet season (May – October) are indicated on each plot by the blue shaded background.

Fig. 4.2 Comparison of monthly accumulated rainfall (mm) observed during the 2006 monsoon season in Niamey Niger by three independent rain gauges: the AMF-

Fig. 5.4 Time-height cross sections of errors in monthly-average temperature profiles simulated by (a) GISS-E2-R and (b) GFDL-CM3, and errors in monthly-average specific humidity profiles simulated by (c) GISS-E2-R and (d) GFDL-CM3. Errors are defined as the difference between the observed value at each level during each month in 2006 and the upper or lower bound of the decadal envelope simulated by each model during 2006 – 2010.

Fig. 5.5 Monthly-mean values for the quantities in Fig. 3.1 versus monthly-mean precipitation as observed by the AMF-1 in 2006 (black triangles) and as simulated during 2006 – 2010 by GISS-E2-R (purple asterisks) and GFDL-CM2 (red open circles). A linear fit to the monthly-means is indicated by solid lines of corresponding color. The value of R^2 reflecting the amount of variance explained by each fit is listed in Table 4.2 for each quantity.

Fig. C.1 Envelopes of minimum and maximum monthly-mean rainfall rate simulated by GISS-E2-R in the grid cells (a) northwest, (b) west, (c) southwest, (d) north, (f) south, (g) northeast, (h) east, and (i) southeast of (e) the grid cell containing Niamey, Niger during the period 2006 – 2010 compared to the values derived from AMF-1 measurements during 2006 in Niamey, Niger.

Fig. C.2 Same as Fig. C.1 except for GFDL-CM3.

Chapter 1: Introduction

1.1 GCM Performance: Capabilities and Challenges

The ability to take the appropriate actions today to mitigate the potentially devastating consequences of anthropogenic influences on Earth's climate system hinges on the level of confidence associated with global climate models (GCMs) used to make projections of future climate change. There is considerable confidence that GCMs make reliable projections of future climate change at continental scales, but significantly less confidence at regional scales (Randall et al., 2007; Flato et al., 2013). GCMs have consistently and univocally predicted climate warming in response to increased greenhouse gas emissions, although they have yet to converge with respect to the magnitude and timing of the predicted warming (IPCC, 2013). These uncertainties present major issues for policy makers. Accordingly, research in atmospheric science is at present largely focused on assisting model developers with the key task of improving GCMs.

A major source of confidence in future projections of climate change is the demonstrated ability of GCMs to simulate observed features of the current climate.

The ongoing effort to improve GCMs over the last few decades has steadily progressed with respect to certain aspects of the observed climate, yet remains grid-locked with respect to others. For example, GCMs have continually demonstrated improved capabilities simulating mean climate features (e.g., the large-scale distributions of temperature, precipitation, winds, and radiation) and many patterns of climate variability (e.g., some major monsoon circulations, seasonal temperature shifts, storm tracks and rain belts, and the Northern and Southern annular modes), yet face long-standing issues simulating tropical precipitation, the El Niño-Southern Oscillation, and many smaller-scale structures (Randall et al., 2007). The poor representation of cloud processes has repeatedly been attached to the limited progress with respect to these and many other long-standing issues with GCM performance (Jakob, 2010). Therefore, the task of improving GCMs for the purpose of increased confidence in making reliable projections of future climate change at small scales, and the magnitude and timing of projected climate change at large scales, primarily translates to the task of improving the representation of clouds and convective processes in GCMs.

There are a number of ways to upgrade the atmospheric component of a present-day GCM formulation, although most upgrades do not guarantee an

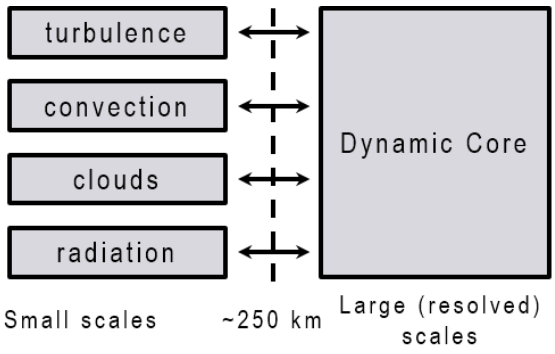

Figure 1.1 Depiction of the interaction between resolved and parameterized unresolved cloud-related processes (convection, turbulence, clouds, and radiation) in present-day climate models (Adapted from Fig. 12.2 in Siebesma et al., 2009).

improved representation of cloud processes. Upgrades to atmospheric models typically made while retaining the current basic architecture of the formulation (depicted in Figure 1.1) include: increasing spatial resolution, increasing complexity through the addition of previously unrepresented processes; and the improvement of the physical basis of existing parameterizations. Increasing spatial resolution and adding complexity to the model formulation by including more processes do not entirely address the fundamental challenges faced representing a majority of cloud processes, and in many circumstances do little to improve or even adversely affect certain aspects of model performance (Illingworth and Bony, 2009). Improving the physical basis of parameterizations is certainly the most direct route to improving the representation of cloud processes, but the last few decades have proven this approach to be difficult and slow to facilitate progress in overall model performance. A few alternative architectures have been explored to improve the representation of model clouds, including: global cloud-resolving models (Satoh et

al., 2008) and super-parameterizations (Grabowski, 2001; Randall et al., 2003). Alternative architectures are too computationally demanding for routine application yet still too coarse to resolve most cloud processes at current operating resolutions (Siebesma et al., 2009). Over the course of the last decade, a consensus is forming that the improvement of the physical basis of existing parameterizations is the most promising way to improve the representation of cloud processes in GCMs (Stephens, 2005; Illingworth and Bony, 2009; Jakob, 2010).

While there is no shortage of important research questions that would contribute to the improvement of existing parameterizations in GCMs, it is not the intention of this work to focus on any single issue in particular. The persistence of these issues after decades of research suggests that perhaps the responses to the increasing pressure to improve model clouds can be made more effective by enhancing the process by which the representation of clouds is improved in GCMs.

1.2 Weak Links in the GCM Development Cycle

The GCM development cycle, schematized in Figure 2, may most basically be described as an iterative process between two well developed sets of activities that essentially occur in isolation (Jakob, 2010). In the first set of activities (represented

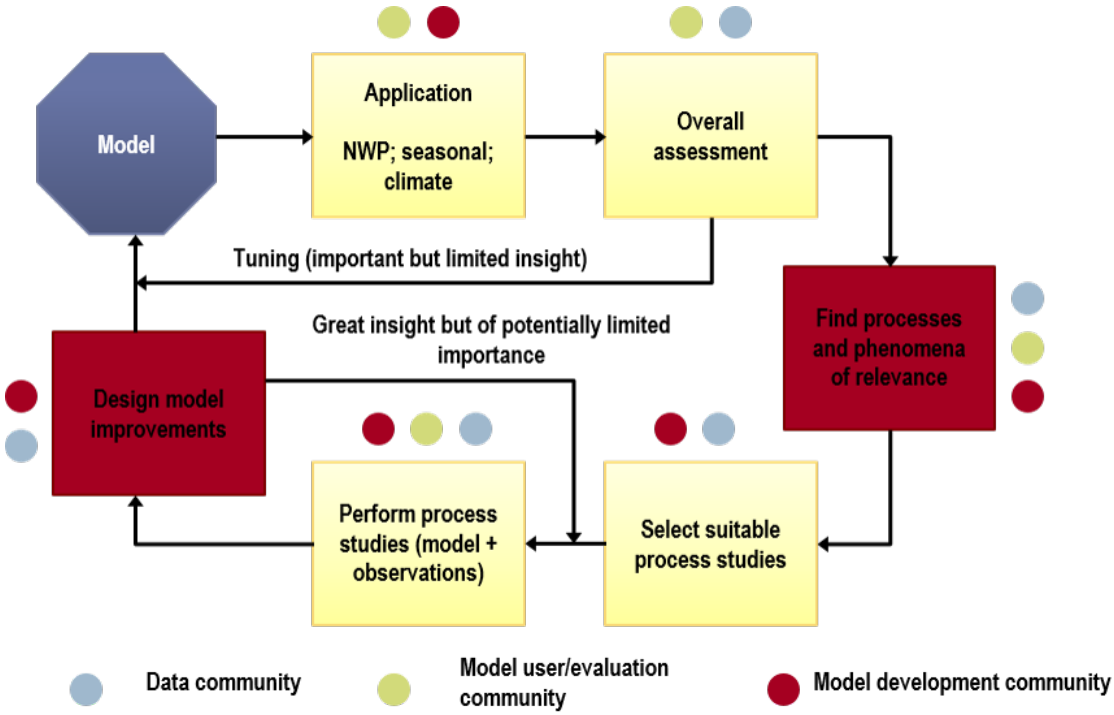

Fig. 1.2 Schematic of the model development process (Adapted from Fig. 1 in Jakob, 2010). Rectangles depict steps in the model development process and circles identify the communities involved in each step. Red rectangles indicate steps that are currently problematic. These problematic steps effectively create weak links in the model development process as a whole, ultimately limiting its efficiency.

by the yellow rectangles in the top half of Figure 2.1), GCMs are subjected to overall performance assessments. Overall performance assessments

are accomplished by comparing grid-scale model output of select climatological variables to global or regional observational datasets acquired primarily from space-based remote sensors. It is from these assessments that model errors and improved capabilities are identified and held in comparison to one another. In the second set of activities (represented by the yellow rectangles in the bottom half of Figure 2), individual parameterizations are improved upon through participation

in offline process studies. Process studies are performed locally, so that detailed observations of relevant variables for a particular process of interest may be obtained. These studies serve to improve understanding of the specific physical mechanisms relevant to a given process and enable the development of parameterizations that are more physically realistic. The GCM development cycle as a whole is most efficient when process studies are selected to directly address the specific aspects of model formulations that are most responsible for overall performance errors. In practice, problems identified by overall performance assessments cannot be definitively linked to the underlying deficiencies in the model formulation. Without definitive guidance about what to fix in the existing formulation, the development of the next generation of models is driven by other motivations. However rational these motivations may be, they often do not address the underlying deficiencies responsible for many of the performance problems identified in the previous model version (Jakob, 2010). As a result, performance issues may persist through multiple development cycles, despite the many improvements incorporated into the formulations with each new generation of models. The capability of GCMs to adequately simulate Sub-Saharan Sahelian rainfall is one example of a very critical performance issue that has lacked a

connection to specific deficiencies in underlying model physics and has resultantly persisted through numerous model development cycles over recent decades.

1.3 Rainfall Predictions in the Sahel

There is high confidence that African ecosystems are already being affected by climate change, and future impacts are expected to be substantial (Niang et al., 2014). In particular, the Sahel has been identified as a hotspot of climate change (Diffenbaugh and Giorgi, 2012) where unprecedented temperature changes are projected to emerge in the later 2030s to early 2040s (Mora et al., 2103). Projected rainfall change over sub-Saharan Africa in the mid- and late 21st century is, however, highly uncertain because climate modelers have yet to establish a consensus with regard to the magnitude and direction of change (Cook and Vizy 2006; Biasutti et al., 2008; Druyan, 2011; Fontaine et al., 2011; Roehrig et al., 2013, Christensen et al., 2013). Lack of confidence in projected rainfall hinders effective decision making in efforts to plan and implement adaptation strategies for this highly vulnerable region.

Intercomparison of coupled GCM simulations indicated no consensus among the models with regards to the future of the West African Monsoon (WAM) system (Cook and Vizy, 2006; Roehrig et al.,2013). An evaluation of the capability

of models from the fifth phase of the Coupled Model Intercomparison Project (CMIP5) to simulate the main features of the WAM indicates that the latest generation of models cannot be relied upon for anticipated climate changes in West Africa, especially with regard to precipitation (Roehrig et al., 2013). At present, low confidence in future projections is partially based on the limited success of CMIP3 and CMIP5 GCMs to simulate the main drivers of the West African monsoon system, such as the observed correlation between Sahel rainfall and basin-wide area-averaged SST variability (Christensen et al., 2013) and partially attributed to non-specific deficiencies in the representation of clouds and convection in GCMs (Niang et al., 2012). As is the case for many other GCM performance issues, what the specific deficiencies are and how to identify them remains unclear.

1.4 Connecting Grid-Scale Performance with Local Sources of Error

By design, traditional model evaluation techniques do not lend their results to interpretation at scales beyond that which they directly evaluate. Overall performance assessments (i.e., evaluations of grid-scale climatological mean quantities) evaluate the spatial distributions of a desired quantity and it relations to other variables identified as large-scale controls through observations. These

studies can therefore identify non-local sources of error in models that don't simulate the observed relationship between a given quantity and its known controls. For example, model inter-comparison studies that evaluate the capability of models to simulate the known features of the WAM in the present-day climate provide valuable information with regards to possible non-local sources of error in the simulation of rainfall in the Sahel, such as SST variability (Niang et al., 2014). While local sources of error are comingled with non-local sources of error, it is not possible to isolate their subgrid-scale origins without a comprehensive assessment of the model physics.

Model physics is typically evaluated by process studies, which evaluate the physical integrity of parameterization schemes offline, using comprehensive datasets made available by field studies in a single location. Unfortunately, this approach is not ideally suited for diagnosing local sources of large-scale performance issues because the model physics is not being tested in the same environment that the large-scale performance issues were originally identified (i.e., within the coupled GCM). While deficient representation of subgrid-scale processes may be diagnosed based on the nature of physical inconsistencies identified by the evaluation, there is no direct way to translate the relevance of these errors with respect to overall

performance, when the parameterization is operating within the GCM. There is currently no alternative approach to model evaluation that is focused on bridging this gap.

Miller et al. (2012) evaluated the seasonal cycle of precipitation and column-integrated cloud-related quantities simulated by four coupled GCMs by comparing standard model output sub-sampled from CMIP3 standard model output to observations from the Radiative Atmospheric Divergence using Atmospheric Radiation Measurement (ARM) Mobile Facility, Geostationary Earth Radiation Budget (GERB) data, and African Monsoon Multidisciplinary Analysis (AMMA) stations (RADAGAST) experiment during 2006 in Niamey Niger. Although the results of this evaluation were not ultimately applied to diagnose local sources of error in the simulation of Sahelian rainfall, this study identified a unique window through which performance evaluations using standard model output could be interpreted in terms of the convective parameterizations employed by each GCM. Expanding this technique with the more fully comprehensive set of observations available from RADAGAST would enable a 'grid-scale process study', from which local sources of error may be diagnosed based on inconsistencies identified by the evaluation of grid-scale model output.

1.5 Goals and Outline

The resolution of long-standing issues with GCM performance, such as those associated with rainfall in the Sahel, may be greatly benefitted by a better understanding of local sources of error. **This study uses a non-traditional method to substantiate the underlying influence of the parameterization of subgrid-scale convective processes on the capability of GCMs to simulate the seasonal cycle of rainfall associated with the WAM and establish a direct connection between the treatment of convective rainfall and overall model performance on seasonal time scales.** Standard model output extracted from CMIP5 emission scenarios of two GCMs will be evaluated during the present period in terms their capability to capture the seasonal cycles and inter-relationships between rainfall, near-surface meteorology, the thermodynamic environment, clouds, and the surface energy balance as observed during the RADGAST experiment in 2006. This unique approach effectively applies the diagnostic technique of a process study to seasonal-scale model output so that convective parameterizations may be evaluated natively, while operating within their respective GCMs. Not only is this method better suited to diagnose local sources of error than traditional methods, it's

comprehensiveness offers a new perspective on the capability of GCMs to simulate the present-day Sahelian climate.

Chapter 2 describes the sources of observations and model output, and the methodology used for direct comparison. Chapter 4 provides as overview of the observations from RADAGAST during 2006. In Chapter 5, the performance of two CMIP5 models is evaluated by direct comparison to the observations presented in Chapter 4. Chapter 6 provides a summary of major finding and discusses the limitations of the method applied in this study.

Chapter 2: Data and Methods

2.1 Observations

2.1.1 The RADAGAST Experiment

The RADAGAST experiment coordinated surface-based measurements from the AMF-1 deployment in Niamey, Niger (13°29'N, 2°10'E) with space-based measurements from Meteosat-8, a geostationary satellite positioned over 0° longitude, collected over the entire seasonal cycle during 2006. The basic measurement geometry of each component is illustrated in Figure 2.1. Meteosat-8 holds the GERB broadband radiometer, which provided measurements of radiative fluxes at the top of the atmosphere, and a multichannel Spinning Enhanced Visible and Infrared Imager (SEVIRI), which was used to derive observations of cloud cover. The GERB

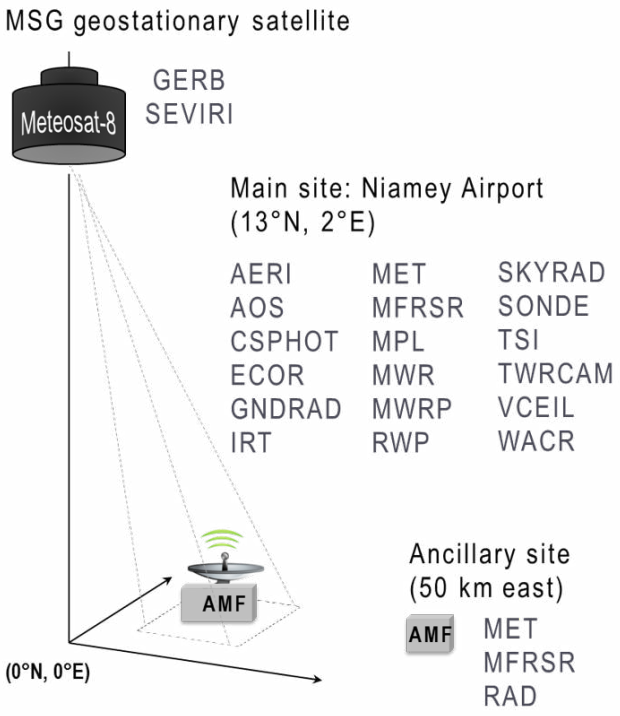

Fig. 2.1 Observational platforms utilized in the RADAGAST experiment.

radiometer is described by Harries et al. (2005) and the SEVIRI imager is described by Schmetz et al. (2002). The AMF-1 provided measurements at the surface (including the surface energy balance and surface meteorology) and of the column directly above (including the atmospheric state, cloud properties and aerosol properties). A full description of the AMF-1 suite of sensors can be found in Mather and Voyles (2013) or Miller and Slingo (2007).

2.1.2 AMF-1 Instrumentation and Primary Measurements

The AMF-1 Surface Meteorology System (MET) contains a suite of conventional in-situ sensors that provide measurements of barometric pressure, temperature, relative humidity, wind speed and wind direction at 1-min resolution. There were three sources of rainfall measurements at the Niamey Airport site. One-minute mean precipitation rate was recorded by the AMF-1 optical rain gauge (ORG) and the AMF-1 Present Weather Detector (PWD). A tipping bucket rain gauge (TBRG) provided cumulative rainfall totals every 5-minutes.

Vertical profiles of atmospheric temperature and humidity were available from radiosondes and a 12-channel microwave radiometer profiler (MWRP). Radiosondes were launched four times daily from the Niamey Airport site, providing in-situ measurements of atmospheric pressure, temperature, and relative

humidity through the extent of the troposphere, sampling every 10 seconds. The MWRP provides vertical profiles of atmospheric temperature and water vapor density at 47 levels from the surface to 10 km at 20-second temporal resolution in all weather conditions except precipitation.

Observations of vertically integrated water vapor (IWV) and the liquid water path (LWP) in the atmospheric column over the site were derived from measurements made by the AMF-1 2-channel microwave radiometer (MWR). The MWR detects atmospheric emissions at 23.8 and 31.4 GHz from water vapor and liquid water directly overhead every 20 seconds with a field of view of 5.9 degrees. IWV and LWP are derived by a statistical algorithm that uses monthly linear regression coefficients determined specifically for Niamey based on *a priori* data from radiosonde soundings (Liljegren, 1999). Uncertainties in the LWP and IWV measurements are ~10 g m^{-2} and 2%, respectively (Revercomb et al, 2003).

Three active remote sensors were utilized to detect cloud boundaries at the AMF-1 site: The W-Band ARM Cloud Radar (WACR), the Micropulse Lidar (MPL), and a laser ceilometer (CEIL). The WACR measures backscatter from signals emitted every 6 seconds at 95 GHz to a range of 18 km with a range resolution of 42 meters. The MPL emits 532-nm signals every 30 seconds and

measures backscatter to 18 km with a range resolution of 30 m. Using a 905-nm pulse emitted every 15 seconds, the CEIL detects backscatter from up to 7.5 km with a range resolution of 15 m.

The AMF-1 Eddy correlation flux measurement system (ECOR) provides observations of surface latent and sensible heat fluxes every half-hour. ECOR contains two instruments, a fast-response, three-dimensional sonic anemometer, and an open-path infrared gas analyzer (IRGA). The sonic anemometer measures three orthogonal wind components and the speed of sound, which is used to derive atmospheric temperature. The IRGA measures water vapor density. All three direct measurements are made at a rate of 10 Hz. Half-hourly observations of latent and sensible heat fluxes are derived from the direct measurements using the eddy covariance technique. Based on the measurement accuracies of the three wind components, the speed of sound, and water vapor density, the expected uncertainties in the latent and sensible heat fluxes are 5% and 6% respectively (Cook and Pekour, 2008).

Upwelling and downwelling irradiances were observed at the surface by the Surface Broadband Solar and Infrared Radiation Station (SIRS) (Stoffel, 2005; Augustine et al., 2000). Shortwave (295 – 3000 nm) and irradiances were measured

by normal incidence pyheliometers and pyranometers at 1-min intervals, and longwave (3.5 - 50μm) irradiances were measured at 1 minute intervals by Eppley precision infrared radiometers.

Table 2.1 Summary of instrument data streams and value-added products from the ARM Data Archive

Data Stream	Originating Instrument(s)	Measurements	Full Date Range
30ecor	Eddy correlation flux measurement system	Latent heat flux	11/26/05 – 1/7/07
		Sensible heat flux	
wacr	W-Band ARM Cloud Radar	Cloud fraction	3/16/06 – 12/29/06
ceil	Ceilometer	Cloud base height	11/23/05 - 1/8/07
gndrad60s	Ground radiometers on stand for upwelling radiation	Longwave broadband upwelling irradiance	11/24/05 – 1/7/07
		Shortwave broadband total upwelling irradiance	
met	Surface meteorological instrumentation	Relative Humidity	11/28/05 – 1/8/07
		Atmospheric Pressure	
		Atmospheric Temperature	
		Horizontal wind	
		Precipitation	
mwrlos	Microwave radiometer	Liquid water path	11/23/05 – 1/8/07
		Precipitable water	
mwrp	Microwave radiometer profiler	Specific humidity	1/9/06 – 1/8/07
		Temperature	
skyrad60	Sky radiometers on stand for downwelling radiation	Longwave broadband downwelling irradiance	11/26/05 – 1/07/07
		Shortwave broadband diffuse downwelling irradiance	
		Shortwave broadband total downwelling irradiance	
sondewnpn	Balloon-borne sounding system	Relative Humidity	1/7/06 – 1/8/07
		Temperature	

Table 2.1 summarizes the instrument data streams available from the ARM data archive that contain the above mentioned measurements that were utilized in this study.

2.2 Climate Models

This study utilizes standard model output from CMIP5 representative concentration pathway (RCP) 4.5 to evaluate the present-day capabilities of two GCMs: National Oceanic and Atmospheric Administration Geophysical Fluid Dynamics Laboratory Global Coupled Model 3 (GFDL-CM3) and National Aeronautics and Space Administration Goddard Institute for Space Studies General Circulation ModelE2 (GISS-E2-R). These two models were specifically chosen based on the availability of documentation related to the formulation of each, and the differences in their respective parameterizations of convection. The formulations of the atmospheric components of GFDL-CM3 and GISS-E2-R are described in Donner at al., (2011) and Schmidt et al. (2014), respectively. Information stated here regarding the representation of convective processes was sourced from the above-mentioned documents and references therein, source code made available by the developing institutions, and personal communications with model developers. Although both models take the same fundamental mass-flux

approach to simulate convection, the complexity and physical basis with which various subgrid-scale convective structures and processes are represented in each model is quite different. A brief description of the formulation of each model as it pertains to simulated rainfall in the Sahel is given below to highlight some of these major differences.

2.2.1 GISS-E2-R

Rainfall simulated by GISS-E2-R originates from the moist convection parameterization and the stratiform cloud parameterization. Moist convection is represented in a single column of grid cells by two entraining updrafts and multiple downdrafts. Convective precipitation originates from convective condensate based on updraft speeds and the assumption of a Marshall-Palmer particle size distribution. Within a single grid cell, detrained convective condensate is ultimately transferred to the large-scale cloud routine (a Sundqvist-type prognostic cloud water scheme.) which produces precipitation only after evaporating all cloud water until a threshold relative humidity is reached. Further details with regards to these parameterizations can be found in Del Genio and Yao (1993), Del Genio et al. (1996), Gregory (2001), Schmidt et al. (2006), Del Genio et al. (2007), and Kim et al. (2011,2012).

2.2.2 GFDL-CM3

In the Sahel, rainfall in GFDL-CM3 originates entirely from the convective parameterization. In contrast to GISS-E2-R, the convective structures in GFDL-CM3 are represented with more realism, but microphysical processes associated with convective rainfall receive limited treatment. Shallow and deep convection are represented separately. Deep convection is represented by deep updrafts, mesoscale updrafts, and mesoscale downdrafts. Precipitation from mesoscale updrafts is determined as exactly one-half of the sum of condensate formed in mesoscale updrafts and condensate transferred from convective updrafts. Further details on the convective parameterization can be found in Donner (1993), Donner et al. (2001) and Wilcox and Donner (2007).

2.3 Observations Corresponding to Standard Model Output

2.3.1 2-D Atmospheric Fields

It was recognized during the RADAGAST experiment that uncertainty arises from sampling issues associated with bringing together point measurements from the surface and area-averaged measurements from space to calculate the radiative flux divergence over Niamey (Settle et al., 2008). This uncertainty was minimized by analyzing continuous measurements as daily averages and limiting the scope of the

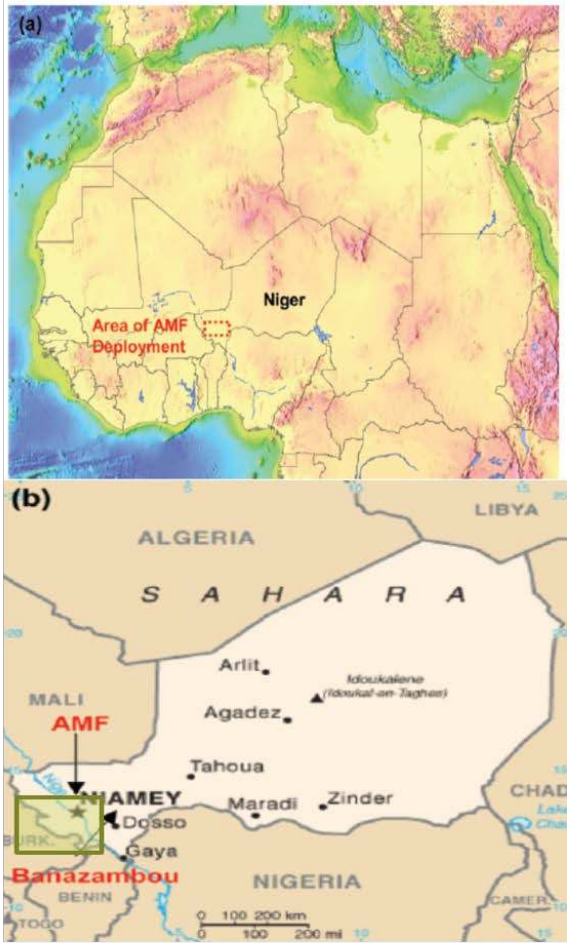

Fig. 2.2 From Fig. 3 in Miller and Slingo, 2007: (a) map of West Africa, and (b) enlargement of the area in Niger where the AMF-1 was deployed. The green-shaded box in the enlargement depicts the 2° latitude by 2.5° longitude footprint of a single column of model grid cells as defined by CMIP5 standard model output.

analysis to the cross-atmosphere radiative flux divergence (Slingo et al., 2008). An analogous issue arises when measurements from the surface are used to evaluate grid-scale GCM output. Figure 2.2 provides a map of northern Africa (top), and an enlargement of the region surrounding Niamey, Niger where the AMF-1 was deployed (bottom). Also indicated by the green box in the enlargement is the footprint of the single column of grid cells from standard model output that includes Niamey. The uniformity of the surface in this region has the very beneficial effect of diminishing spatial variability and the observed surface meteorological and radiative properties were determined to reflect regional aspects of the West African monsoon, making such measurements from the AMF during RADAGAST suitable for the evaluation of GCMs in terms of their ability to simulate the monsoon

circulation (Miller et al., 2009). The applicability of column-integrated measurements of the radiatively active constituents of the atmosphere (i.e., water vapor, clouds, and aerosols) and measurements of the vertical structure of cloudiness and the thermodynamic environment within the atmosphere are relatively less certain (Miller et al., 2012). However, it is promising that daily-averaged measurements of aerosol optical thickness were found to be highly correlated between the main site in Niamey and the auxiliary site 50 km away (Miller et al., 2009) and results that rely on cloud mask data to determine clear and cloudy conditions showed essentially no sensitivity as to which cloud mask was used (Slingo et al., 2009). Limitation of the proposed analysis to monthly-averaged quantities further supports the applicability of column-integrated quantities.

2.3.2 Thermodynamic Profiles

In this study we combine measurements from a ground-based profiling microwave radiometer and collocated radiosondes to generate atmospheric temperature and humidity observations that are tailored to the thermodynamic profiling requirements of atmospheric model development applications. To establish the suitability of microwave radiometry for such application, the thermodynamic profiling capability of a 12-channel microwave radiometer was evaluated against

collocated radiosonde observations for extended time periods in a variety of climatological regimes, including continental and marine environments in the subtropics and mid-latitudes. For the purpose of representing a vertical column of grid cells in an atmospheric model, in each of the climatological regimes studied, thermodynamic profiles derived from radiometric retrievals were achievable with an accuracy similar to that of radiosondes. To demonstrate the utility of combined profiles for model development applications, a high-resolution data product was generated using radiometric retrievals to fill in the gaps between radiosonde soundings and applied to evaluate thermodynamic profiles from a similar high-resolution data product that was generated using model output to fill in the gaps between radiosonde soundings. A full description of this methodology is given in Chapter 3.

Chapter 3: High Resolution Thermodynamic Profiles for Atmospheric Model Development

Atmospheric temperature and humidity measurements that are used to develop, evaluate, and initialize the atmospheric community's entire hierarchy of models are almost exclusively acquired by radiosondes. However, the spatial and temporal characteristics of radiosonde observations are poorly suited for modeling applications, which would benefit most from zenith volumetric measurements that are representative of atmospheric grid cell volumes. Atmospheric models can have 50 to 200 vertical layers and physics time steps on the order of minutes to an hour. Radiosonde soundings are a series of point measurements, collected over the course of a couple of hours as the balloon ascends through the atmosphere. Limited by cost, equipment, and staffing, it is not routinely feasible to launch more than two radiosondes per day for extended periods of time. Observations that are more representative of a vertical column of model grid cells may be derived from measurements made by zenith-pointing ground-based remote sensors, including

microwave radiometers, infrared radiometers, and LIDARs. While relatively coarse vertical resolution does not restrict the utility of these measurements for modeling applications, vertical range limitations and operability constraints are more problematic, to varying degrees. With no alternative measurement technique capable of all-weather thermodynamic profiling throughout the depth of the atmosphere, radiosondes remain of crucial importance.

Exclusive reliance on radiosondes for observations of thermodynamic profiles limits the efficiency of the model development process, particularly with respect to the improvement of the representation of clouds and convection. The lack of thermodynamic measurements that are directly comparable to model output on time scales appropriate for cloud and convective processes compounds the difficulty of effectively diagnosing model deficiencies. Although the use of radiosondes will be necessary for the foreseeable future, the atmospheric community could benefit greatly by incorporating remote sensor measurements to more closely achieve the thermodynamic profiling requirements of modeling applications.

Ground-based microwave radiometry is a well-established technique for thermodynamic profiling of the troposphere (Hogg et al., 1983; Solheim et al., 1998a; Westwater 1993; Westwater et al., 2005). Commercially available

microwave profilers are capable of long-term, unattended, daytime/nighttime equivalent operation in all weather conditions except moderate to heavy precipitation, and may be used to derive near-continuous vertical profiles of temperature and humidity with vertical resolution on the order of hundreds of meters from the surface to 10 km. These attributes make ground-based microwave profilers uniquely appealing for modeling applications, for which high temporal resolution is desired and moderate vertical resolution is acceptable (Liljegren et al., 2001).

Capable of observing both non-dramatic and rapidly changing thermodynamic variations in the lower troposphere (Güldner and Spänkuch, 2001; Knupp et al., 2009), radiometric profiles can be used to fill in the gaps between radiosonde launches. Although vertical resolution degrades linearly with height in the boundary layer and more rapidly above (Cimini et al., 2006; Cadeddu et al., 2013), evaluations of a 12-channel profiling microwave radiometer conducted in Lindenberg, Germany (Güldner and Spänkuch, 2001), and in Lamont, Oklahoma, and Barrow, Alaska (Liljegren et al., 2001) show that thermodynamic profiles acquired from radiometric retrievals and radiosonde observations are of similar accuracy when applied to represent the atmospheric volumes defined by weather

forecast model grid cells (Ware et al., 2003). Based on these studies, the primary utilization of radiometric retrievals has been for data assimilation purposes with the goal of improving short-term forecasts from numerical weather prediction models.

It has been recognized that measurements from microwave profilers may be of similar benefit when used to drive single column models and cloud resolving model simulations during model development field studies (Liljegren et al., 2001). The Atmospheric Radiation Measurement (ARM) Program has operated a 12-channel microwave radiometer profiler (MWRP) as part of its first ARM Mobile Facility (AMF1) since 2005. The AMF1 is a portable atmospheric laboratory that includes a suite of remote and *in situ* sensors designed to collect data in under-sampled climatologically important regions which may be used by the atmospheric community to evaluate climate and process models (Miller and Slingo, 2007; Mather and Voyles, 2013). The extensive dataset available from the AMF1 MWRP presents a unique opportunity to investigate the application of radiometric retrievals to atmospheric model evaluations.

In this study we present a practical method for obtaining adaptable, high-resolution thermodynamic profiles that are suitable for application in atmospheric

model evaluations by combining measurements from a ground-based profiling microwave radiometer with co-located radiosonde observations. First, to establish the use of microwave radiometry for this purpose, data are used from six AMF1 deployments to show that accurate radiometric retrievals are attainable in climate regimes most relevant to atmospheric model development. We then use combined radiometric retrievals and radiosonde observations from a single AMF1 deployment to evaluate a model-based radiosonde-related data product to demonstrate the advantages of adequate high-resolution thermodynamic profiles for atmospheric model development.

3.1 Methods

This study utilizes data from the six AMF1 deployment locations summarized in Table 3.1. The deployments varied in duration from six to 19 months, collectively providing 66 months of data between 2005 and 2013. Clear and cloudy conditions in polluted and clean air masses are represented in a diverse set of climatologies from under-sampled regions throughout the Northern Hemisphere.

Table 3.1. Selected AMF1 Deployment Periods and Locations

Deployment Location	Site ID	Lat,Lon [°N,°E]	Elev. [m]	Dates
Point Reyes, CA	PYE	[38.1, -123.0]	24	Mar. - Sep., 2005
Niamey, Niger	NIM	[13.5, 2.2]	223	Jan - Dec., 2006
Black Forest, Germany	FKB	[48.5, 8.4]	511	Apr. - Dec., 2007
Shouxian, China	HFE	[32.6, 116.8]	23	May - Dec., 2008
Graciosa Island, Azores	GRW	[39.1,-28.0]	26	May 2009 - Dec. 2010
Cape Cod, MA	PVC	[42.0,-70.0]	43	Jun. 2012 - Jul. 2013

The AMF1 was first deployed in 2005 at Point Reyes National Seashore (PYE) on the northern coast of California for a period of six months. PYE is characterized by the frequent presence of marine stratocumulus clouds and drizzle that are typical for marine west coast climates. For the calendar year of 2006 the AMF1 was deployed in Niamey, Niger (NIM) in the West African Sahel. NIM is located in a semi-arid region dominated by the West African Monsoon and subject to one of the largest moisture gradients on Earth. In 2007 the AMF1 was in the mountainous Black Forest region of Germany (FKB) for a period of nine months. This region receives a significant amount of orographic precipitation. For 8 months in 2008 the AMF1 was in Shouxian, China (HFE), located outside a rural town surrounded by farmland. During 2009 and 2010 the AMF1 was deployed on Graciosa Island in the Azores (GRW). Located on the border between the subtropics and mid-latitudes, GRW represents a unique remote marine

environment. For a period of 12 months during 2012 and 2013 the AMF1 was deployed in Cape Cod, Massachusetts (PVC).

The AMF1 deployment history provides an ideal dataset for the purposes of this study. NIM, PYE, and GRW are located in regions with environmental conditions that present challenges for the operation of remote sensors, and climatologies that are critical to the development of atmospheric models. The characterization of the capabilities of profiling microwave radiometers in these three locations is crucial for establishing the utility of the sensor for atmospheric model evaluation. The mid-latitude deployments in HFE, FKB, and PVC represent climatologies where profiling radiometers have been most frequently used, and therefore serve as a good comparison of the AMF1 MWRP performance capabilities to that of other studies.

The AMF1 MWRP, Radiometrics Corp. TP/WVP-3000, uses a tunable frequency synthesizer in the receiver to sequentially measure atmospheric radiance [$W \cdot m^{-2} \cdot sr^{-1} \cdot \mu m^{-1}$] expressed as brightness temperatures [K] at 5 K-Band and 7 V-Band frequencies between 20 and 60 GHz (Solheim et al., 1998a). In this frequency range, atmospheric emission is dominated by water vapor, atmospheric oxygen, and cloud liquid water. The K-Band (water vapor sensing) frequencies

(22.035, 22.235, 23.835, 26.235, 30.0) and V-Band (temperature sensing) frequencies (51.25, 52.28, 53.85, 54.94, 56.66, 57.29, and 58.8 GHz) were selected based on eigenvalue analysis (Solheim et al., 1998b). The calibration of the water vapor channels is monitored monthly and updated when necessary using the tipping curve calibration method (Liljegren, 2000; Han and Westwater, 2003). Temperature sensing channels are calibrated every three to four months with liquid nitrogen (LN_2). The radiometric accuracy of observed brightness temperatures is 0.5 K, although it can be 1 - 2 K in the transparent oxygen channels where the LN_2 calibration is less accurate (Cadeddu et al., 2013). Measurement is impeded when liquid water on the antenna radome results in artificially high brightness temperatures. A blower system is used to minimize the accumulation of liquid water on the radome and a rain sensor provides a flag for potentially contaminated data. Additional sources of error include artificially high brightness temperature measurements resulting from observations in directions that are within 15° of the solar zenith angle and "spikes" caused by radio frequency interference.

Vertical profiles of temperature and humidity are derived from brightness temperature measurements using a statistical inversion method that is based on historical radiosonde data specific to each deployment location and a radiative

transfer model. The microwave radiative transfer model (Schroeder and Westwater, 1991) uses the Rosenkranz (1998) absorption model for oxygen and water vapor, modified for a narrower half-width of the 22 GHz water vapor line (Liljegren et al., 2005, Garnache and Fisher, 2003) and for the MT-CKD water vapor continuum (Mlawer et al., 2003). Due to the exponential nature of the weighting functions in the retrieval algorithm (Askne and Westwater, 1986), vertical resolution of retrieved profiles based strictly on information provided by the brightness temperature measurements is relatively coarse: 100 m (500 m) for temperature (water vapor density) achieved within the first kilometer, and degrades rapidly above (Cadeddu et al., 2013). However, the fine vertical resolution contributed by historical radiosonde data allows for thermodynamic profiles to be provided approximately every 20 seconds for 47 vertical layers from the surface to 10 km, with 100-m resolution from the surface to 1 km and 250-m resolution from 1 to 10 km.

3.2 Comparison with radiosondes

Utility for profiling radiometers in atmospheric modeling evaluation is founded upon the suitability of radiometric retrievals for combination with radiosonde observations. This suitability specifically translates to the capability

to retrieve thermodynamic profiles at high temporal resolution for extended periods of time with minimal interruption and consistent accuracy that is comparable to radiosonde observations in a diverse set of relevant climate regimes. In the following we test the performance and quantify the accuracy of thermodynamic profiles derived from measurements made by the AMF1 MWRP during the six deployments identified in Table 3.1.

The number of profile comparisons for each deployment is summarized in Table 3.2. All available data was used from the entire length of each deployment, however, the number of profile comparisons was impacted by the availability of both radiosonde observations and radiometric retrievals, and particular site climatology. MWRP hardware malfunctions were responsible for significant periods of missing radiometric retrievals, collectively reducing the number of total available comparisons by ~1000. Dew-blower malfunctions eliminated ~30 days in PYE and ~100 days in GRW. Failed surface

Table 3.2. Number of MWRP-Radiosonde Comparisons at selected AMF1 Deployments

Site ID	Duration [Months]	Number of Comparisons
PYE	6	392
NIM	12	1322
FKB	9	629
HFE	8	713
GRW	19	1074
PVC	12	588
TOTAL	66	4718

meteorology sensors eliminated ~60 additional days in GRW. Especially humid and/or precipitating conditions further reduced the number of available comparisons at each site to varying degrees. Systematic filtering for these conditions accounted for the loss of 1 % of available comparisons in NIM, 5 % in HFE, 16% in PVC and FKB, and 20% in PYE and GRW.

Vertical profiles of temperature and humidity derived from measurements made by the AMF1 MWRP were evaluated against co-located SONDE observations. For each profile comparison, SONDE observations were linearly interpolated to match the vertical resolution of the MWRP, and the first available single radiometric retrieval within a half-hour of the SONDE launch time was selected. Statistics of the discrepancies between the MWRP and SONDE (defined as MWRP - SONDE) observations approximate the accuracy of radiometric retrievals at each deployment location.

The mean discrepancies (biases) and root-mean-square discrepancies (RMS errors) between the MWRP and SONDE are presented in Fig. A1 for each AMF1 deployment. Radiosonde errors typically assigned by the National Centers for Environmental Prediction (NCEP) when assimilating radiosonde observations into numerical weather models (www.emc.ncep.noaa.gov/gmb/bkistler) are plotted

against the MWRP RMS errors for comparison (black lines). These errors serve as an expression of the uncertainty that arises when using point measurements from radiosondes to represent grid cell average values in atmospheric models.

For temperature profiles, the MWRP exhibits a small positive bias near the surface and a negative bias above 2 km that is relatively larger in magnitude and peaks near 7 km (Fig. 3.1-a). In terms of surface rainfall occurrence, the driest locations, NIM and HFE, exhibited the smallest biases, both within 1 K to 10 km. FKB and PYE had the largest biases, with magnitudes of ~2 K near the surface and ~3 K aloft. MWRP RMS errors in temperature (Fig. 3.1-b)

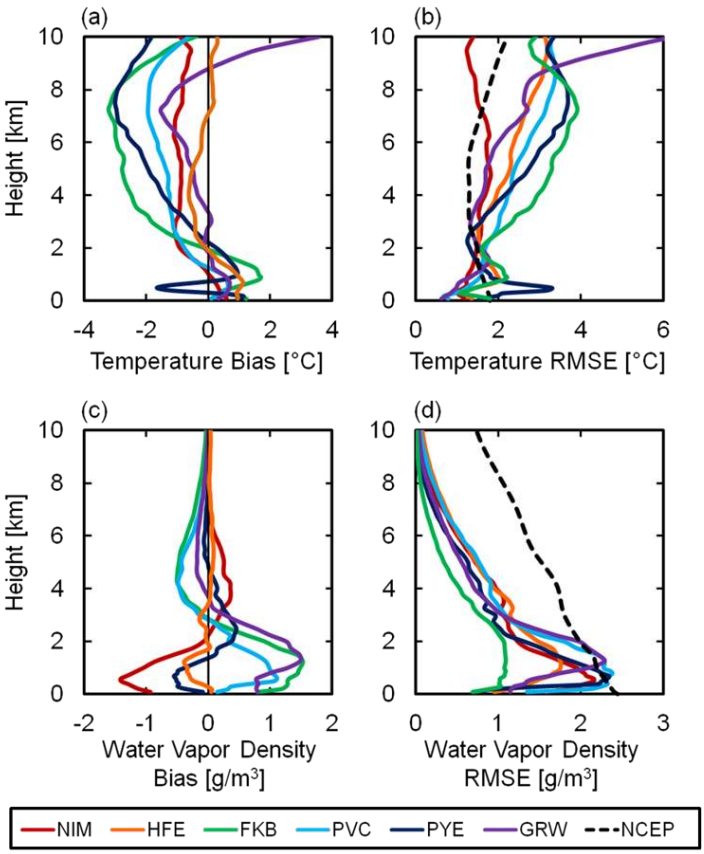

Fig. 3.1. Accuracy of thermodynamic profiles derived from the microwave radiometer profiler (MWRP) estimated by statistical comparisons with co-located radiosonde observations (SONDE) while deployed as part of the Atmospheric Radiation Measurement (ARM) program's first ARM Mobile Facility (AMF1)* between 2005 and 2013. Temperature profile errors are presented as (a) mean (bias) and (b) root-mean-square (RMS) discrepancies (defined as T_{mwrp} - T_{sonde}) for AMF1 deployments in Niamey, Niger (NIM, red), Shouxian, China (HFE, yellow), Black Forest, Germany (FKB, green), Cape Cod, Massachusetts (PVC, light blue), Point Reyes, California (PYE, dark blue), and Graciosa Island, Azores (GRW, purple). RMS discrepancies are compared to errors typically assigned by the National Center for Environmental Prediction (NCEP) to radiosonde observations when used in numerical weather model applications (black dashed line). Plots (c) and (d) are the same as (a) and (b), except for water vapor density in $g \cdot m^{-3}$.

range between 1 and 2 K from the surface to approximately 4 km and degrade to a maximum value between 1.5 and 4 K at about 7 km. Some notable exceptions to the general trend were found at NIM, PYE, and GRW. For NIM, RMS errors did not degrade to a maximum value near 7 km, but were maintained within 2 K throughout the profile. RMS errors at PYE follow a trend similar to that of the other sites except near a height of 0.5 km, where RMS errors of about 3 K are uncharacteristically large. To a height of 6 km, RMS errors at GRW are similar in magnitude to NIM, but then degrade continuously with height to about 6 K at 10 km.

For water vapor density profiles, the MWRP has a negative bias (Fig. 3.1-c) near the surface and a positive bias aloft at drier locations (NIM, HFE, and FKB), while the three wetter locations shown the opposite trend, although all are within 2 $g \cdot m^{-3}$. RMS errors in water vapor density were remarkably consistent among the six locations. Near the surface errors are about 1 $g \cdot m^{-3}$, then reach a maximum value that is less than 2.5 $g \cdot m^{-3}$ before 2 km, and then continuously decrease with height. For all sites, MWRP RMS errors are roughly equivalent to or less than radiosonde errors at all sites from the surface to 10 km. The only

notable exception to the general trend was found at FKB, where RMS errors are maintained within about 1 $g \cdot m^{-3}$ from the surface to 10 km.

Example vertical profiles of temperature from the MWRP and SONDE are compared for each of the AMF1 deployment locations in Table 3.1.

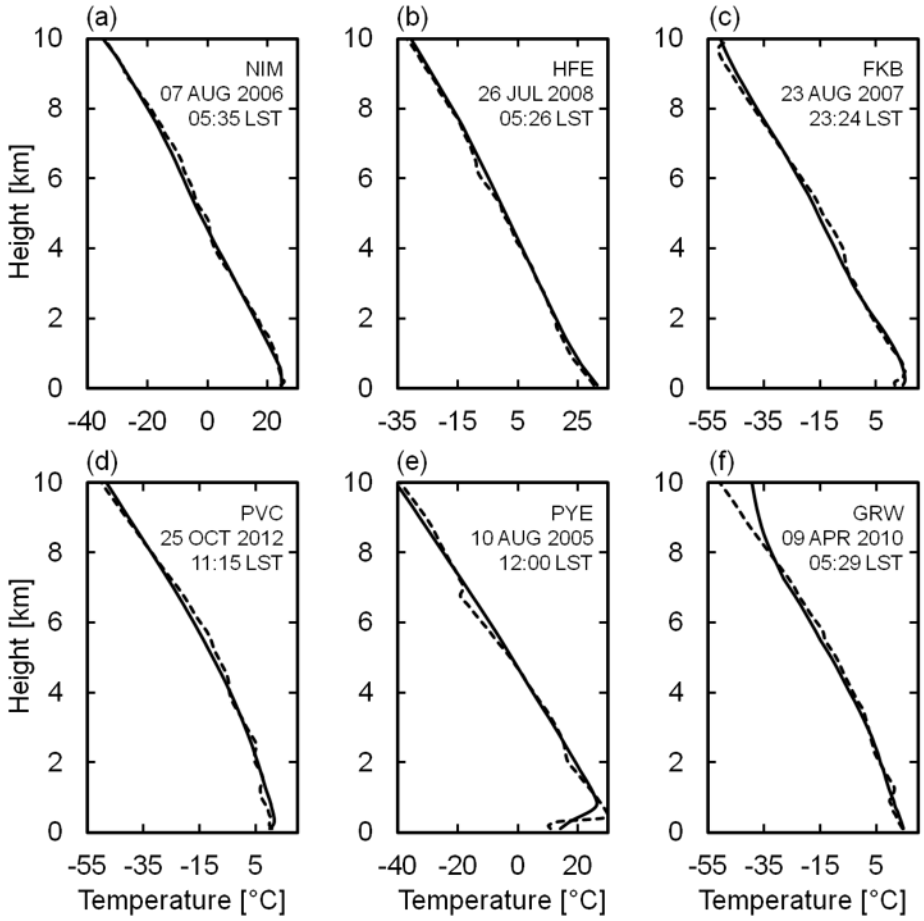

Fig. 3.2. Example vertical profiles of temperature in °C from the MWRP (solid lines) and SONDE (dashed lines) from (a) NIM on 07 August 2006 at 05:35 LST, (b) HFE on 26 July 2008 at 05:26 LST, (c) FKB on 23 August 2007 at 23:24 LST, (d) PVC on 25 October 2012 at 11:15 LST, (e) PYE on 10 August 2005 at 12:00 LST, and (f) GRW on 09 April 2010 at 05:29 LST.

Disagreement between the MWRP (solid lines) and SONDE (dashed lines) profiles is almost exclusively associated with the presence of temperature inversions. While weak surface inversions are captured by the MWRP relatively well (Fig. 3.2-a) and 3.2-c), discrepancies arise in proportion to the magnitude of the inversion strength for all inversions above 0.5 km (Figs. 3.2-a to 3.2-f). This suggests that the range in temperature RMS errors among the different climatological regimes is primarily due to the height, strength, and persistence of temperature inversions at each site, and is consistent with the decreasing vertical resolution of the MWRP and the RMS temperature errors presented in Fig. 3.1. At PYE, for example, the strong temperature inversion near 0.5 km (Fig. 3.2-e) was persistent throughout the length of the deployment and can be directly associated with the peak in temperature RMS errors for PYE near 0.5 km (Fig. 3.1-b). The discrepancy between the MWRP and SONDE above 8 km at GRW (Fig. 3.2-f) is not associated with a temperature inversion, however is a consistent problem given the high temperature RMS errors found in this portion of the profile at RW (Fig. 3.1-b). This is most likely the result of an issue with the regression coefficients in the retrieval algorithm generated from historical radiosonde data, but would need to be investigated.

Example vertical profiles of water vapor density from the MWRP and SONDE are compared for each of the AMF1 deployment locations in Fig. 3.3. Disagreement between the MWRP and SONDE is very much the result of the coarse vertical resolution of the MWRP and sharp moisture gradients in the lower portions of the atmosphere. As was found with the temperature profiles, the general trend of water vapor density with height is well represented in observations from the MWRP, within the realm of possibility given the limited vertical resolution of the radiometric retrievals.

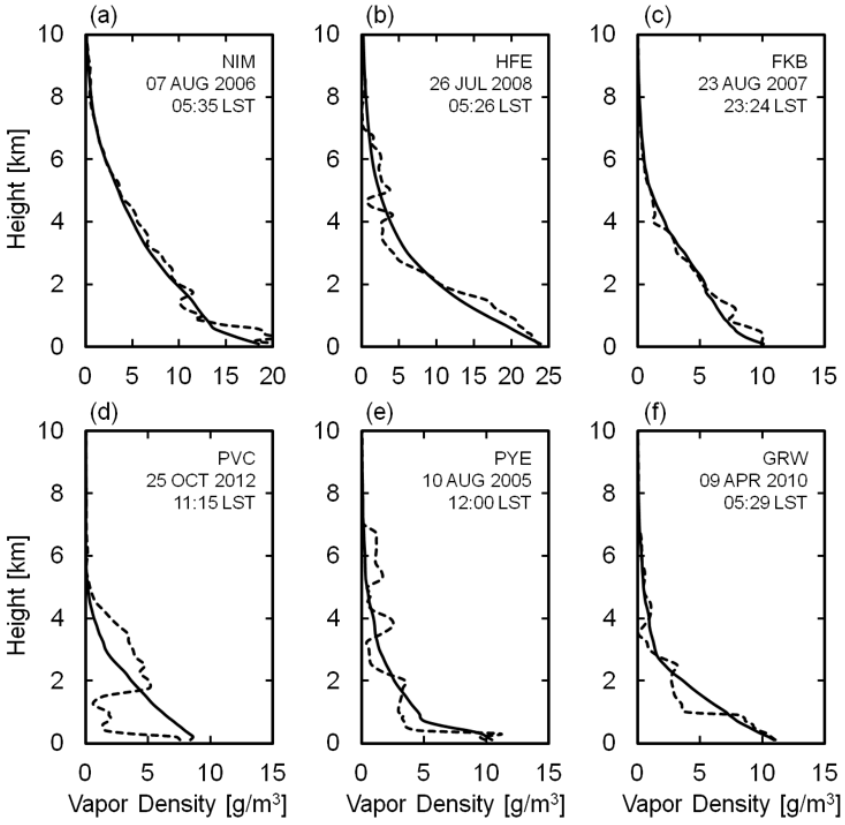

Fig. 3.3. Same as Fig. 3.2, except for water vapor density in $g \cdot m^{-3}$.

Our findings establish a unique potential for ground-based microwave radiometry to provide sufficiently reliable and accurate thermodynamic profiles with spatial and temporal resolutions that are appropriate for atmospheric modeling applications. Radiometric retrievals from the MWRP were evaluated against co-located SONDE observation for extended time periods using data from six AMF1 deployment locations that represent the marine and continental environments in the sub-tropics and mid-latitudes. Overall, RMS errors in temperature ranged 1 - 2 K from the surface to about 4 km and 1 - 4 K to 10 km and RMS errors in water vapor density were within 2.5 $g \cdot m^{-3}$ from the surface to 10 km. These errors are similar to the uncertainty that NCEP assigns to point measurements from radiosondes when they are used to represent grid cell average values in weather prediction models.

MWRP RMS errors in temperature and humidity at HFE, FKB, and PVC were equivalent to or slightly larger than reported by Güldner and Spänkuch (2001), Liljegren et al. (2001), and Cimini et al. (2006) using a similar retrieval method with an identical radiometer in similar mid-latitude climatologies. Larger errors may be accounted for by the longer duration (greater than six months) of each AMF1 deployment in comparison to the much shorter time periods (three to

six months) utilized by prior studies. The longer deployment periods in the present study encompass a broader range of operating conditions within each climate regime. In addition, calibration of the MWRP was most likely better maintained during prior studies due to closer monitoring of the instrument. The variability of RMS errors in temperature among each AMF1 deployment site was also slightly larger than reported by Westwater et al. (2000) for four different North American environments, although the current dataset included a more diverse set of climatologies.

For the purpose of meeting the thermodynamic profiling requirements of atmospheric modeling applications, the performance of the MWRP at NIM, PYE, and GRW is generally promising, yet exposes some challenges. MWRP RMS errors in temperature and humidity at these locations were equal to or smaller than those from HFE, FKB, and PVC. In NIM, the MWRP operated almost continuously without interruption for a period of twelve months. However, in the marine environments of PYE and GRW, although interruptions from rainfall were general brief, three instances involving hardware malfunctions primarily associated with the dew blower caused substantial gaps in data availability from periods ranging for about one month to nearly three months. Close monitoring and mitigation

plans for anticipated hardware complications would have to be in place to acquire long-term continuous datasets in marine environments.

Having demonstrated the profiling capabilities of the MWRP in a diverse set of climatologies that are specifically relevant to atmospheric modeling development, we conclude that thermodynamic profiles derived from measurements made by the MWRP are best exploited for atmospheric modeling applications when used in combination with radiosonde soundings.

3.3 Model evaluation using combined profiles

Radiosondes and radiometers have a complementary set of advantages with respect to modeling applications that enables a uniquely effective synergy between the two instruments that is readily adaptable to the specific thermodynamic profiling requirements of model evaluations. To illustrate this potential, radiometric retrievals and radiosonde observations are used in combination to validate the Merged Sounding (MERGESONDE) Value-Added Product (VAP) (Troyan, 2012) (referred to hereafter as MS_{ecmwf}), a model-based radiosonde-related data product. MS_{ecmwf} profiles are typically used as input for higher order VAPs, but have also been used for research applications requiring thermodynamic profiles

at high temporal resolution to study the relationships between thermodynamics, clouds, and precipitation in West Africa (Kollias et al., 2009).

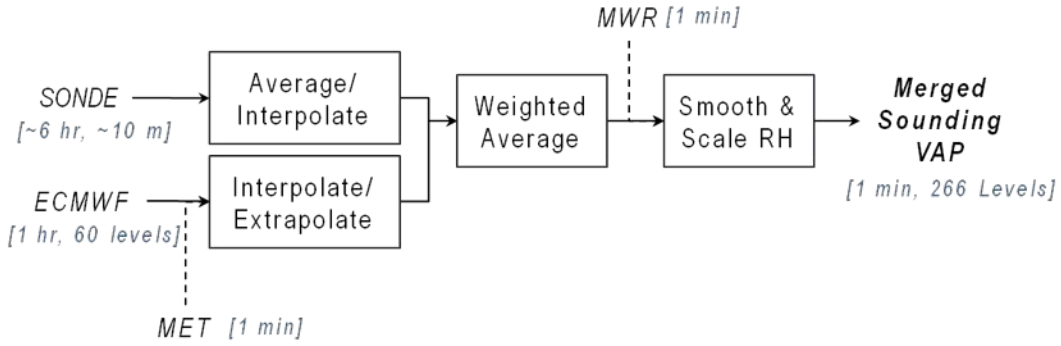

Fig. 3.4. MS_{ecmwf} flow chart.

MS_{ecmwf} provides thermodynamic profiles for 266 levels from the surface to 20 km at 1-min temporal resolution by merging radiosonde observations with hourly ECMWF model output. As illustrated in Fig.3.4, the merge algorithm first interpolates radiosonde observations and model output onto separate, but common profile grids. The profiles are merged based on the temporal proximity to the nearest radiosonde observation using a double-sigmoid weighting function to determine the weight each profile contributes to the merged product. Radiosonde observations are given a 100% weight at the time of observation, near 05:30, 11:30, 17:30, and 23:30 UTC each day. ECMWF output has a maximum weighting in between radiosonde observations, near 02:30, 08:30, 14:30, and 20:30 UTC. Surface

meteorological instrumentation (MET) and a two-channel microwave radiometer (MWR) provide 1-min observations that serve as boundary conditions at the surface and scale the relative humidity profiles, respectively.

To evaluate MS_{ecmwf} thermodynamic profiles, a similar MWRP-Merged Sounding (MS_{mwrp}) data product was created using the same algorithm, but 1-min radiometric retrievals are used in place of hourly ECMWF output. Boundary conditions provided by MET and the MWR in MS_{ecmwf} were not applied. Above 10 km, where radiometric retrievals are not available, radiosonde observations are simply interpolated. MS_{mwrp} was generated using observations from the AMF1 deployment in Niamey, Niger during 2006. Thermodynamic profiles have the same spatial and temporal resolution as MS_{ecmwf}.

Time-height cross-sections of temperature and relative humidity from MS_{ecmwf} and MS_{mwrp} for 11 August 2006 are compared in Fig. 3.5. Below 10 km, there are significant differences in the evolution of temperature throughout the day. The four vertical streaks in MS_{ecmwf} occur at the times when the model output is weighted most heavily. The model output and SONDE observations are not in good agreement, and the observed structure is a result of the weighted average used to merge the two data sources. The MWRP and SONDE agree rather well

and produce a much more realistic evolution of temperature. Relative humidity structures are, however, remarkably similar below 10 km.

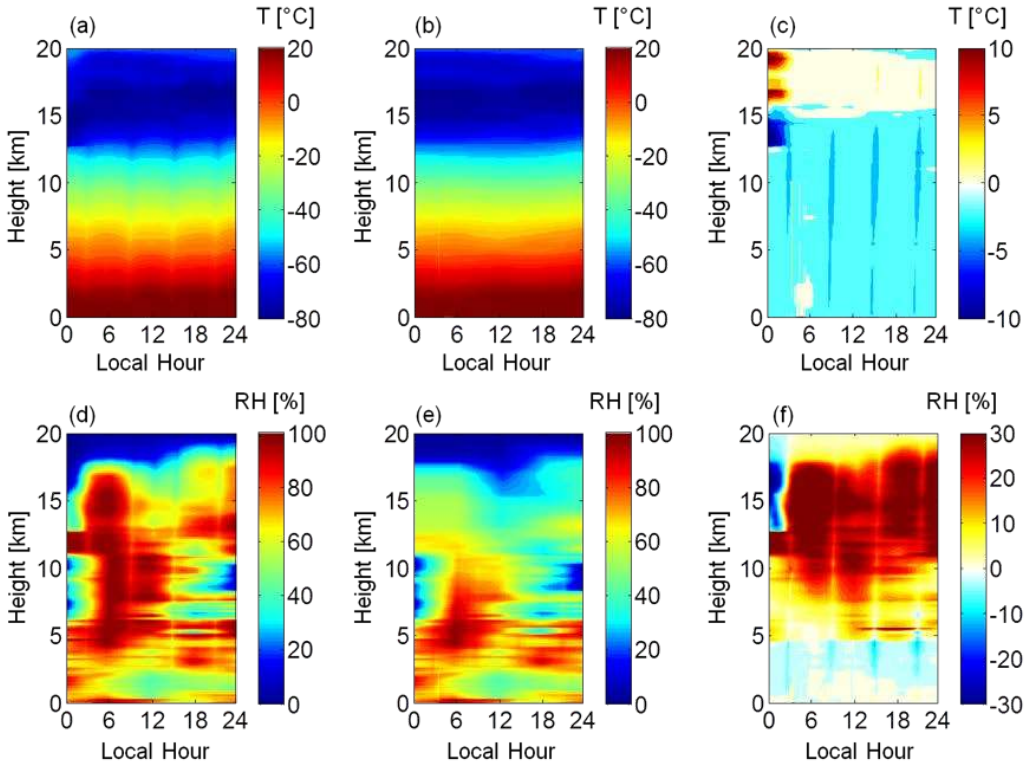

Fig. 3.5. Time-height cross sections of temperature in °C for August 11, 2006 in Niamey, Niger from the (a) MS_{ecmwf} and (b) MS_{mwrp} high-resolution radiosonde-related data products, and (c) the temperature discrepancy between the two products, defined as MS_{ecmwf} - MS_{mwrp}. Plots (d) - (f) are the same as (a) - (c), except for relative humidity in %. MS_{ecmwf} was generated by combining radiosonde observations with ECMWF model output. MS_{mwrp} was generated using an identical algorithm, except that vertical profiles of temperature derived from the AMF1 MWRP were used in place of model output.

Above 10 km, where no high resolution data is available to fill the gaps between radiosonde launches in the MS_{mwrp} product, the evolution of temperature agrees rather well with the MS_{ecmwf} product. In contrast, the evolution of relative humidity differs significantly between the two data products, with much higher relative

humidity values in the MS_{ecmwf} product. The incorporation of model data to fill the gaps between radiosonde launches in the MS_{ecmwf} product appears to have a greater influence on the evolution of relative humidity than for temperature above 10 km. This suggests that only having available high resolution data from the surface to 10 km in the MS_{mwrp} product may be more of a limitation for relative humidity than for temperature.

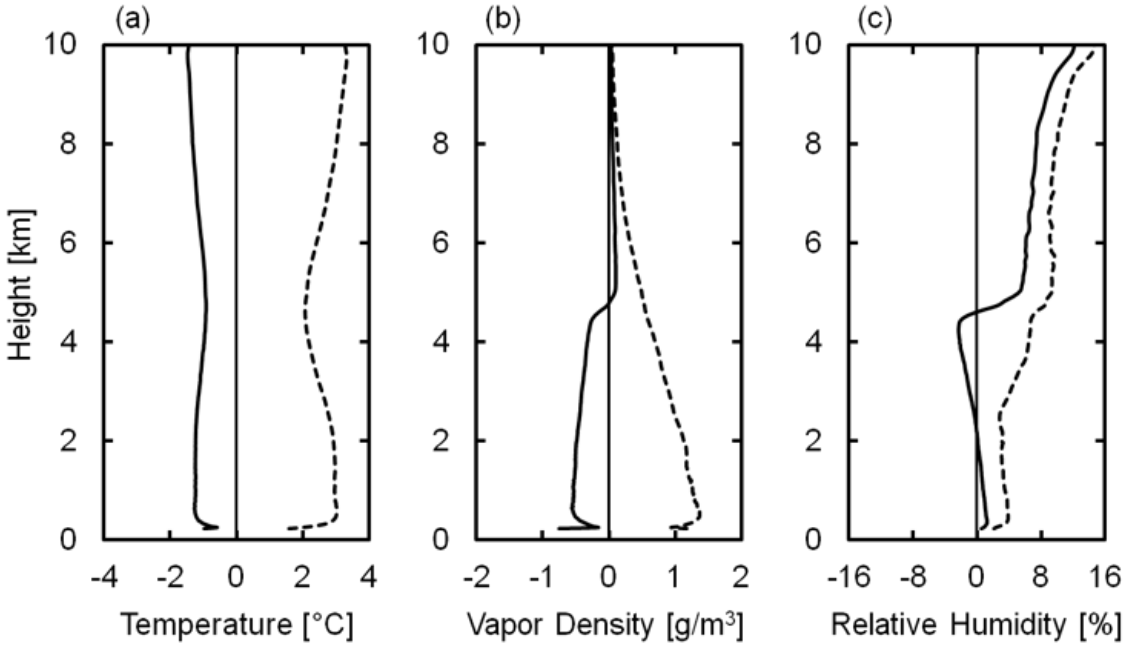

Fig. 3.6. Bias (solid lines) and RMS error (dashed lines) in MS_{ecmwf} profiles of (a) temperature in °C, (b) water vapor density in g/m^3, and (c) relative humidity in % for the six-month period of May through October of 2006 in Niamey, Niger.

Mean and RMS discrepancies in temperature, water vapor density, and relative humidity between MS_{ecmwf} and MS_{mwrp} (defined as MS_{ecmwf} - MS_{mwrp}) for the

2006 monsoon season are shown in Fig. 3.6. MS_{ecmwf} exhibits a negative temperature bias of about 1 K from the surface to 10 km (Fig. A6-a). The RMS difference is 1.5 K near the surface, and 2-3 K to 10 km. These differences are larger than the MWRP RMS error determined for the year 2006. For water vapor density, MS_{ecmwf} shows a small negative bias, within -0.5 g m^{-3}, to 5 km, and a slight positive bias, within 0.2 K from 5 to 10 km (Fig. 3.6-b). RMS differences are within 1.5 g m^{-3} from the surface to 10 km, which is roughly equivalent to MWRP RMS errors for the year 2006. MS_{ecmwf} and MS_{mwrp} compare extremely well for relative humidity from the surface to 5 km, with negligible bias and RMS differences within 5% (Fig. 3.6-c). Above 5 km, MS_{ecmwf} tends to be increasingly more humid with height, although RMS differences are within 15% to 10 km. These results are consistent with the differences identified between the two data products in the August 11, 2006 example from the surface to 10 km.

High-resolution thermodynamic profiles allow for the investigation of relationships between the thermodynamic environment and other meteorological phenomena that evolve on short time scales, such as cloud cover, precipitation, and radiation. For such applications it is common to characterize the thermodynamic environment in terms of derived quantities, such as convective available potential

energy (CAPE) and convective inhibition (CIN). Due to the complex definition of these quantities, it is not immediately clear how the interpretation of CAPE and CIN may be influenced by uncertainties in the temperature and humidity profiles from which they have been derived. In the following analyses, we compare time series of CAPE and CIN computed using temperature and humidity profiles from MS_{ecmwf} and MS_{mwrp} to determine the implications that uncertainties in temperature and humidity profiles from MS_{ecmwf} may have for the utility of time series of CAPE and CIN derived from this product.

Vertical profiles of temperature and humidity from MS_{ecmwf} and MS_{mwrp} were used to compute CAPE and CIN for the 2006 monsoon season in Niamey, Niger using simple, psuedoadiabatic parcel theory, as described in Appendix A.

The diurnal and seasonal cycles of CAPE and CIN for the 2006 wet season in Niamey, computed from each time series, are compared in Figure 3.7. With respect to the diurnal cycle, MS_{mwrp} values for CIN and CAPE (black lines) range from 0.1 to 0.2 $kJ \cdot kg^{-1}$ and 1.2 to 1.6 $kJ \cdot kg^{-1}$ respectively. CIN tends to a maximum around 6:00 local time (LT) and a minimum around 15:00 LT, while CAPE shows an opposing trend, with a maximum at night and a minimum in the morning. The diurnal cycles of CAPE and CIN from the MS_{ecmwf} data product (red

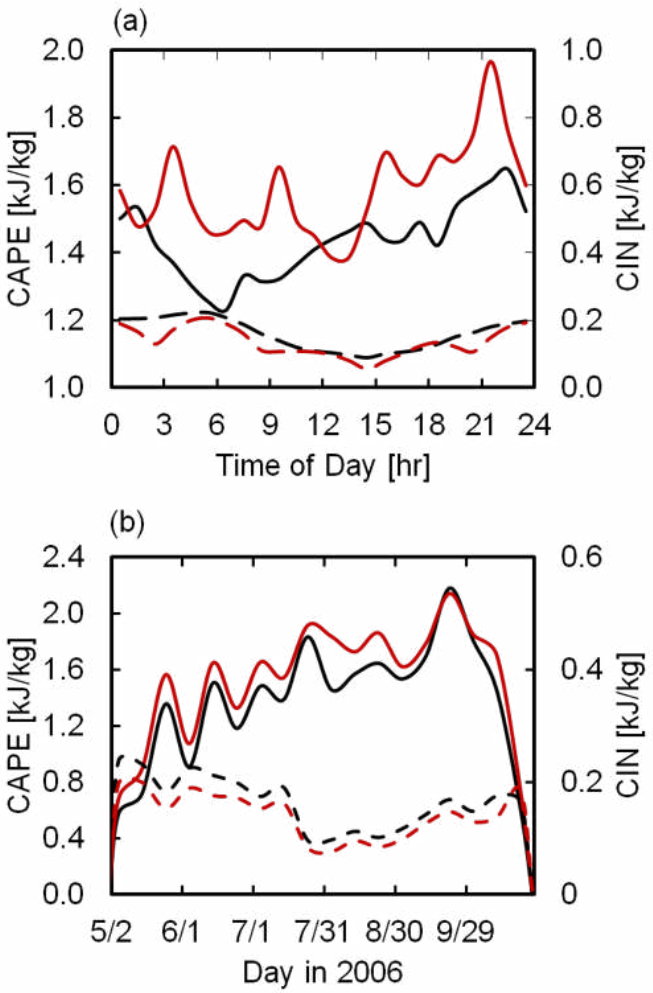

Fig. 3.7. Comparison of (a) diurnal and (b) seasonal cycles of CAPE (solid lines) and CIN (dashed lines) in kJ/kg derived from MS_{ecmwf} (red lines) and MS_{mwrp} (black lines) for the six-month period including May through October of 2006.

lines) are similar, but not as well defined. The evolution of CIN from the MS_{ecmwf} product is almost identical to that of the MS_{mwrp} product, but deviates to lesser values at the times of day when ECMWF output is weighted most heavily by the merge algorithm. CAPE values from MS_{ecmwf} range from 1.4 to 2.0 $kJ \cdot kg^{-1}$, which is generally higher than the MS_{mwrp} range, and the evolution of CAPE throughout the day does not coincide with MS_{mwrp} as well as it does for CIN.

With respect to the seasonal cycles of CAPE and CIN, the MS_{ecmwf} product exhibits a consistent positive bias for CAPE and negative bias for CIN, however, the evolution of both CAPE and CIN are well correlated. Both products show that on average CAPE increases over the course of the monsoon season, starting at approximately 0.5 $kJ \cdot kg^{-1}$ in May and maximizing at 2.0 $kJ \cdot kg^{-1}$ near the end of September, before disappearing entirely at the end of October. Similar values of CAPE were found by Monkam (2002) using low resolution thermodynamic profiles at mandatory levels. Kollias et al. (2009) reported 6-day running mean values of CAPE computed using equivalent potential temperature profiles derived from MS_{ecmwf} temperature and humidity that showed no steady increase in CAPE over the course of the monsoon season, and maintained a substantially higher value of 5 $kJ \cdot kg^{-1}$ throughout. This scale bias limits application of the MS_{ecmwf} VAP for process studies on scales consistent with model time steps and cloud-scale parameterization physics.

These results suggest that the MS_{ecmwf} VAP produces reliable trends for CIN and CAPE on seasonal time scales, but cannot be used to draw relationships between the thermodynamic environment and clouds or precipitation on shorter time scales.

Temperature profiles from the MS_{ecmwf} VAP serve as a data source for the Continuous Baseline Microphysical Retrieval (MICROBASE) VAP (Dunn et al., 2011) to generate vertical profiles of cloud microphysical properties that are in turn used by higher-order VAPs to generate estimates of atmospheric heating rates. The MICROBASE VAP employs a mixed-mode phase partitioning scheme and a set of empirical relationships to derive vertical profiles of liquid water content (LWC), ice water content (IWC), cloud droplet effective radius (R_e) and ice cloud particle effective radius (R_{ei}) from cloud radar reflectivity and ambient temperature. In the following analyses, we use the uncertainty in the MS_{ecmwf} VAP temperature profile δT, estimated by statistical comparison with the MS_{mwrp} data product for the 2006 wet season in Niamey to quantify the uncertainty in the cloud microphysical properties that MICROBASE supplies to higher-order VAPs. Uncertainty equations (Appendix B) are formulated using the log-derivative method and used to demonstrate how the uncertainty propagation resulting from MS_{ecmwf} temperature biases potentially impacts microphysical parameters computed when MS_{ecmwf} temperature profiles are used.

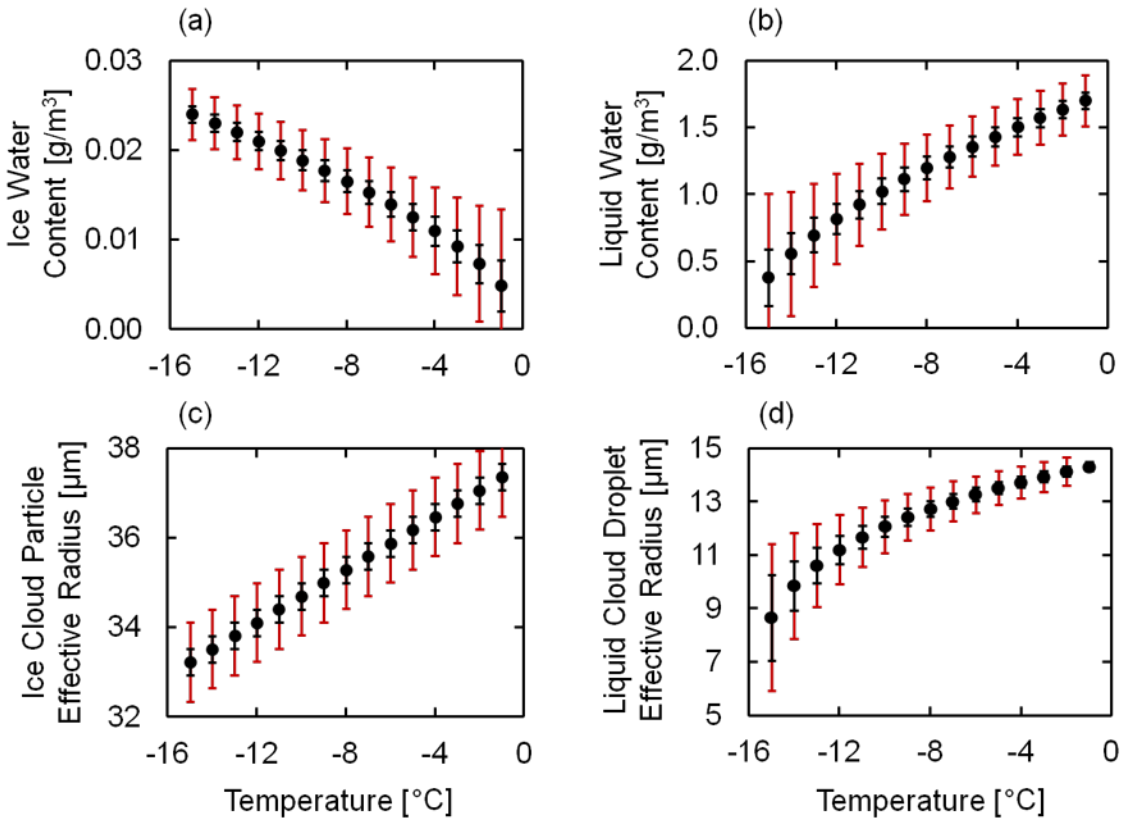

Fig. 3.8. Temperature dependencies of (a) ice water content in g/m^3, (b) liquid water content in g/m^3, (c) ice cloud particle effective radius in µm, and (d) liquid cloud droplet effective radius in µm as defined in the MICROBASE VAP algorithm assuming a total radar reflectivity factor of -10 dBZ. Error bars represent the variability resulting from a 3 °C (red) and 1 °C (black) uncertainty in input temperature profiles.

These results identify a significant sensitivity to uncertainty in the temperature profile with respect to the liquid cloud droplet effective radius in mixed phase clouds in the MICROBASE algorithm. Reductions in temperature-profile specification uncertainties are found in all four microphysical variables computed in MICROBASE (Fig. 3.8). The most significant uncertainty in IWC due to temperature specification is realized when temperatures are near freezing and the

uncertainty in R_{ei} is not temperature dependent. Liquid cloud parameters become progressively more uncertain as the temperatures approach -16 °C, which is the temperature at which MICROBASE assumes that liquid is no longer present in the cloud. These uncertainties in the liquid water parameters are a particularly caustic issue when they are used as inputs to radiation transfer calculations, so any reduction in the uncertainties is highly desirable.

Evaluating parameterizations in atmospheric models is a challenging endeavor because observations are often incomplete and incompatible with model vertical, horizontal, and temporal resolution. A crucial aspect of any model forecast is the thermodynamic profile because it is integrally related to switches within the model that toggle various parameterizations on and off. Invoking the convective parameterization or diagnosing stratiform cloudiness is a function of the predicted thermodynamic profile, for example, and diagnosing the existence and phase of clouds within the model column is also a function of this profile. Many past efforts to evaluate model thermodynamic profiles have relied upon comparisons between radiosonde profiles collected every few hours and the predicted thermodynamic profile. But radiosonde thermodynamic profiles are detailed snapshots, while model calculations in a given grid cell are the result of

the convergences and divergences within the models dynamic core; there is an inherent mismatch between the two profiles. Noting every small fluctuation in the vertical profile of temperature or water vapor during a radiosonde ascent provides little that is directly comparable, by itself, with model output. Of more utility is a continuous, lower resolution thermodynamic profile that mocks model output in temporal and spatial resolution. The MWRP uses detailed radiation transfer calculations operating through a mathematical inversion to produce a continuous estimate of the temperature and water vapor profiles. These profiles often gloss-over specific details such as sharp inversions in favor of an averaged profile, which is quite similar to the behavior of the dynamic cores in models, which do not possess the vertical and temporal resolution to produce anything more.

Beyond the thermodynamic profile as a direct model comparison tool is the temperature sensitivity of microphysical retrievals that are used to evaluate model parameterizations. These retrievals operate continuously and require temperature information to specify the phase of hydrometeors within clouds. Demonstrations presented herein suggest that a combined MWRP and radiosonde thermodynamic profile (MS_{mwrp}) provides a superior product relative to a radiosonde and model derived product (MS_{ecmwf}). Despite the 10-km height limitation imposed when using

the MWRP measurement between soundings, structures in the lower 10-km are better resolved when the MWRP is used and it is in these layers where convective and stratiform cloud parameterizations generally operate. Perhaps most importantly, the specifications of the MS_{mwrp} product deem it more compatible with the requirements for evaluation of GCM thermodynamics and process-related parameterizations.

3.4 Summary and Conclusions

Creating, evaluating, and improving model cloud parameterizations is of critical importance for virtually all types of atmospheric models, and a particularly urgent issue for global climate models (GCMs). This study demonstrates that radiosonde observations and measurements from a profiling microwave radiometer may be combined to provide thermodynamic profiles that are substantially more appropriate for atmospheric model evaluations than radiosonde observations alone.

The accuracy of vertical profiles of temperature and humidity derived from measurements made by the AMF-1 MWRP was estimated by an extensive statistical comparison with co-located radiosonde observations during the course of six deployments between 2005 and 2013. To our knowledge, this is the most extensive and wide ranging comparison to date. It was determined that

thermodynamic profiles suitable for combination with radiosonde observations are attainable from measurements by the MWRP among the diverse set of climate regimes relevant to atmospheric model development. This result establishes a unique potential for high-resolution thermodynamic profiles derived from the combination of radiosondes and radiometers that can be of substantial benefit to the atmospheric community for use in model evaluations.

Some specific results of this study deserve special mention. Combining radiosonde and numerical model output to produce a continuous thermodynamic profile is a useful technique, but it suffers from the need to juxtapose two sources of information that are somewhat dissimilar and requires the use of techniques to meld them together even when they exhibit considerable disagreement. The melding process produces artifacts in the final output product that are clearly evident when the product is compared to a merged product consisting of two types of measurements: radiosondes and the MWRP. Artifacts in the radiosonde and model product propagate into hybrid quantities such as CAPE and CIN, which are important parameters in cloud parameterizations, and these artifacts may mask the true relationships between CAPE and CIN and cloud development that need to be better quantified if they are to be used in cloud parameterizations. Finally,

these artifacts introduce unnecessary uncertainty into downstream algorithms that are sensitive to accurate specification of temperature such as microphysical retrievals.

High-resolution thermodynamic profiles generated by combining measurements from a profiling microwave radiometer and radiosonde observations show potential to enhance the efficiency of the atmospheric model development process, especially with respect to the improvement of the representation of clouds and convection. The capability to quantify the uncertainty of model thermodynamic variables can lead to a better understanding of the sensitivity of model physics to changes in the thermodynamic profile. It is likely that reductions in the uncertainty of model thermodynamics can lead to a narrowing of the variability among different model solutions. A profiling microwave radiometer is a valuable addition to the suites of remote sensors at research facilities with model development missions and we recommend that it become a standard instrument at all sites with this mission.

Chapter 4: Observations

4.1 Background Climatology

The lower troposphere in the Sahel region is a transitional zone between the warm, moist savanna to the south and the hot, dry Sahara Desert to the north. The transition occurs abruptly along a quasi-stationary Intertropical Front (ITF) and is experienced at the surface by sharp meridional gradients in temperature and humidity, and a discontinuity in wind direction. Northeasterly Harmattan winds allow Saharan air to penetrate the portion of the Sahel north of the ITF, while the portion south of the ITF is penetrated by relatively cooler, moist air fronm the tropical Atlantic Ocean. The Sahel is a semi-arid climate zone that experiences two distinct seasons annually, fundamentally driven by the West African Monsoon (WAM) circulation. During the boreal winter the ITF is stationed near 10°N, bringing hot, dry conditions to the Sahel. In spring, the ITF begins a slow northward migration reaching approximately 20°N in mid-August, during which time the Sahel receives a majority of its annual rainfall. The ITF then rapidly retreats southward, and conditions in the Sahel are once again dry by November.

At approximately 13.5°N and 2°E, Niamey, Niger is located near the southern border of the West African Sahel region. The ITF typically passes northward of Niamey (using the standard criteria of 15 °C of sustained near-surface dew point temperatures) during the first dekad in April and passes southward during the last dekad in October (Lélé and Lamb, 2010). Although the monsoon season spans a period of six months, Niamey receives a majority of its rainfall during a core period from later July to early September (Slingo et al., 2007).

4.2 Overview of Observations from RADAGAST

4.2.1 Rainfall

The evolution of monthly accumulated rainfall measured using the AMF-1 PWD during 2006 is shown in Fig. 3.1(a). Rainfall begins modestly in May, steadily increases to a maximum in August, before rapidly declining back to dry conditions in November. Niamey received a total of 386 mm of rain from May through October of 2006, a majority of which (337 mm) occurred during the peak monsoon months of July, August, and September. Although the monthly accumulated rainfall total for August was close to average, below normal monthly accumulations were experienced in all other wet season months (Lélé and Lamb, 2010).

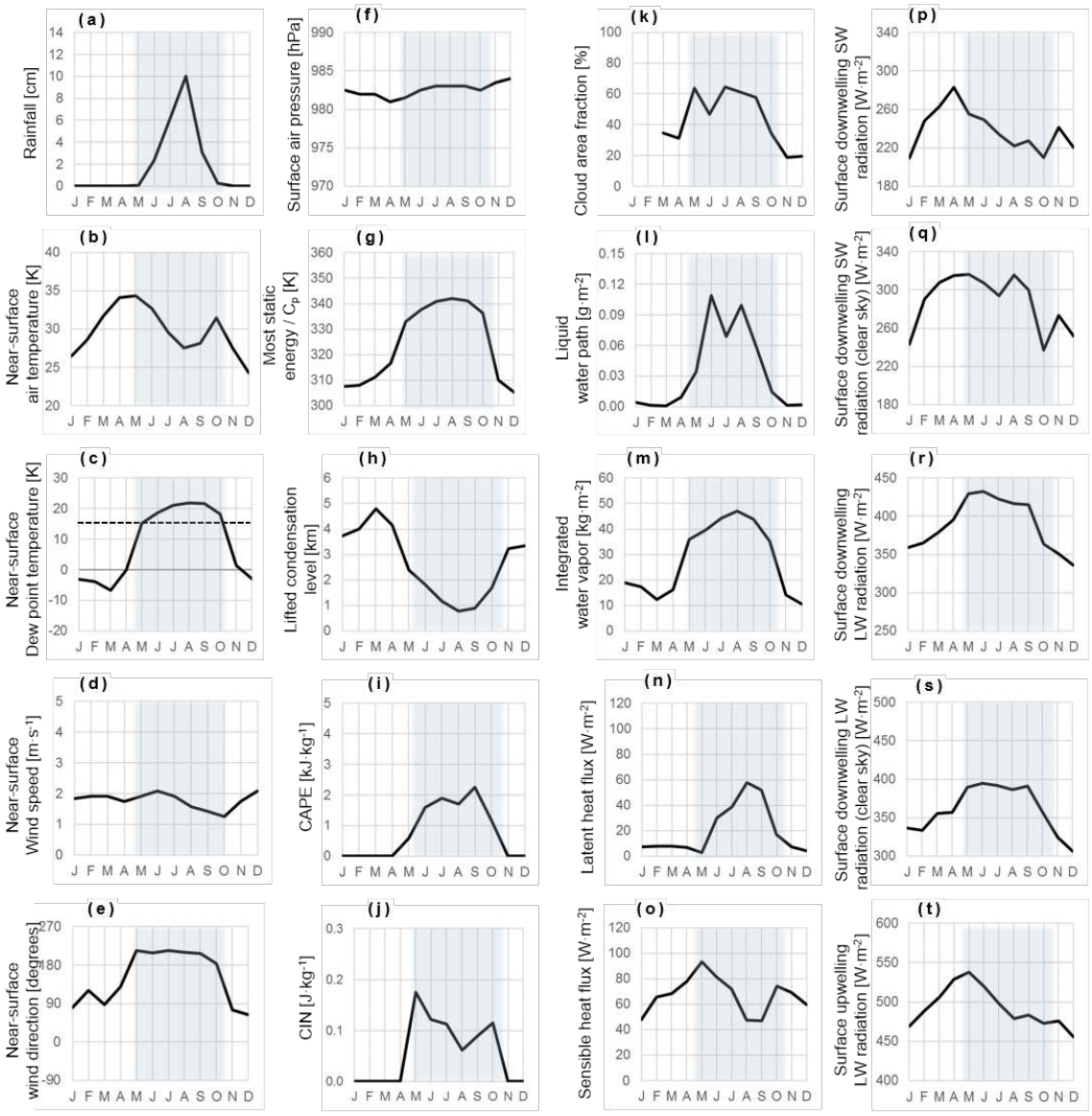

Fig. 4.1 Time series of monthly-mean (a) accumulated rainfall, (b) near-surface air temperature, (c) near-surface dew point temperature, (d) near-surface wind speed and (e) wind direction, (f) surface barometric pressure, (g) near-surface moist static energy, (h) lifted condensation level (LCL), (i) convective available potential energy (CAPE), (j) convective inhibition (CIN), (k) cloud area fraction, (l) liquid water path (LWP), (m) integrated water vapor, (n) surface latent heat flux, (o) surface sensible heat flux, (p) surface downwelling shortwave (SW) radiation, (q) surface downwelling SW radiation for clear sky conditions, (r) surface downwelling longwave (LW) radiation, (s) surface downwelling LW radiation for clear sky conditions, and (t) surface upwelling LW radiation derived from AMF-1 measurements at the Niamey Airport site during 2006. Months included in the 2006 wet season (May – October) are indicated on each plot by the blue shaded background.

Rainfall totals determined from the AMF-1 PWD disagreed with the amounts reported by Slingo et al. (2008), Miller et al. (2009), and Miller et al. (2012) (referred to as S08, M09, and M12 respectively) (Table 4.1).

Table 4.1 Comparison of monthly accumulated rainfall (mm) in Niamey, Niger during 2006 as reported by prior studies and various independent rain gauges.

Month	AMMA TBRG (S08)[1]	AMMA TBRG	AMF-1 ORG (M09)[2]	AMF-1 ORG (M12)[3]	AMF-1 ORG	AMF-1 PWD
Jan	0.0	0.0	1.5	4.3	0.0	0.0
Feb	0.0	0.0	0.0	0.0	0.0	0.0
Mar	0.0	0.0	0.0	0.0	0.0	0.0
Apr	0.0	0.0	0.0	0.0	0.0	0.0
May	1.2	0.6	4.1	4.2	0.1	1.5
Jun	41.1	43.3	17.4	18.9	17.2	41.8
Jul	112.7	102.9	75.3	170.3	74.9	111.2
Aug	183.6	159.1	132.2	132.9	131.9	171.7
Sep	56.4	67.5	46.9	47.3	46.7	55.1
Oct	0.0	8.1	4.1	4.2	4.0	4.9
Nov	0.0	0.0	0.3	0.3	0.0	0.0
Dec	0.0	0.0	0.0	0.0	0.0	0.0
Total	395	381	282	382	276	386

[1] Slingo et al. (2008)
[2] Miller et al. (2009)
[3] Miller et al. (2012)

Using an AMMA TBRG, S08 reported rainfall totals in May through September, with an annual total of 395 mm. Using the AMF1 ORG, M09 reported May through September monthly rainfall totals that are consistently less than S08 throughout the monsoon season, resulting in an annual rainfall amount that is roughly 100 mm less than S08. Also, Rainfall was observed in October and

November according to M09, while no rainfall was reported during these months by S08. To resolve these inconsistencies for the present study, the rainfall rates recorded by the AMF1 ORG were compared to the AMF-1 PWD and an AMMA TBRG located at the Niamey airport site. Close inspection of the 1-minute rainfall rates recorded by the ORG and PWD revealed two major rain events were reported by the ORG were false readings associated with two attempts to recalibrate the instrument. Serial communication errors and dropouts during heavy rainfall were identified in the PWD data throughout the monsoon season. Once corrections for these errors were made, the ORG and PWD data streams were found the be highly correlated (R = 0.98), although measurements from the ORG were about 15% lower than those of the PWD on a consistent basis. Based on a comparison with 5-minute accumulated rainfall recorded by the AMMA TBRG it was concluded that the ORG underreported rainfall. Therefore, monthly accumulated rainfall totals used in this study were derived from measurements by the

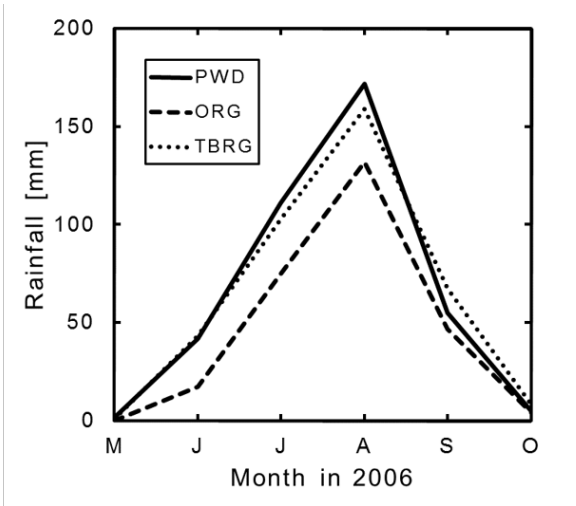

Fig. 4.2 Comparison of monthly accumulated rainfall totals (mm) as observed by three independent rain gauges in Niamey, Niger during the period from May through October 2006.

PWD. Monthly accumulated rainfall totals for the 2006 season from each instrument are shown in Fig. 4.2.

4.2.2 Surface Meteorology

Monthly-mean near-surface air temperature and near-surface dew point temperatures are presented in Fig. 4.1(b) and (c), respectively. Average dew point temperatures are above 15 °C during May through October, defining the 2006 wet season. There are two local maxima in near-surface air temperature over the course of the year, coincident with the beginning and end of the wet season. These results are consistent with the evolution of daily-mean screen-level temperature and dew point temperatures reported by Slingo et al. (2008).

Month-mean near surface wind speeds and directions are shown in Fig. 4.1 (d) and (e), respectively. Although wind speeds remain fairly constant throughout the year, the near-surface wind direction abruptly shifts from northeasterly to southwesterly at the beginning of the wet season. Southwesterly winds are maintained throughout the wet season, and abruptly shift back to northeasterly at the start of the dry season. These results are consistent with evolution of daily-mean surface wind speed and direction reported by Slingo et al. (2008).

Monthly-mean surface air pressure remains fairly constant throughout the year (Fig. 4.1(f)), with a minimum occurring just before the onset of the monsoon season and a less pronounced minimum at the end.

Near-surface air temperature and specific humidity measurements from the AMF-1 MET were used derive surface moist static energy at 1-min resolution ($h = C_p T_s + L_v q_s$). Monthly-mean values of moist static energy divided by C_p (Fig. 4.1(g)) abruptly increase at the start of the wet season, then steadily increases before abruptly dropping back to dry season values at the end of the wet season. These results are consistent with daily-mean values based on measurements by the AMF-1 eddy correlation instrument report by Miller et al. (2009).

4.2.3 The Thermodynamic Environment

Monthly-mean vertical profiles of relative humidity and temperature from the MWRP-MERGESONDE data product described in Chapter 3 are shown in Fig. 4.3(a) and (b), respectively. The presence of the monsoon air mass is evident during May through October in Fig. 4.3(a), and monthly-average relative humidity is highest (~70%) through 5 km during the peak season from July to September. A moderate level of humidity is present in the upper atmosphere for the remained of the year, with the exception of December, during which time the total

atmospheric column is remarkably dry. Although the seasonal cycle of monthly average temperature is fairly uniform throughout the year, there are a few subtle characteristics worth noting. First, the two near-surface temperature maximum identified in Fig. 4.1(b) at the very beginning and very end of the monsoon season are shown to extend upward from the surface to about 1 km. Second, the freezing level remains fairly constant at about 4 km throughout the entire seasonal cycle. Lastly, the effects of peak monsoon season deep convection on the temperature profile are reflected in the warming of the atmosphere near 18 km, which is most pronounced during the month of August.

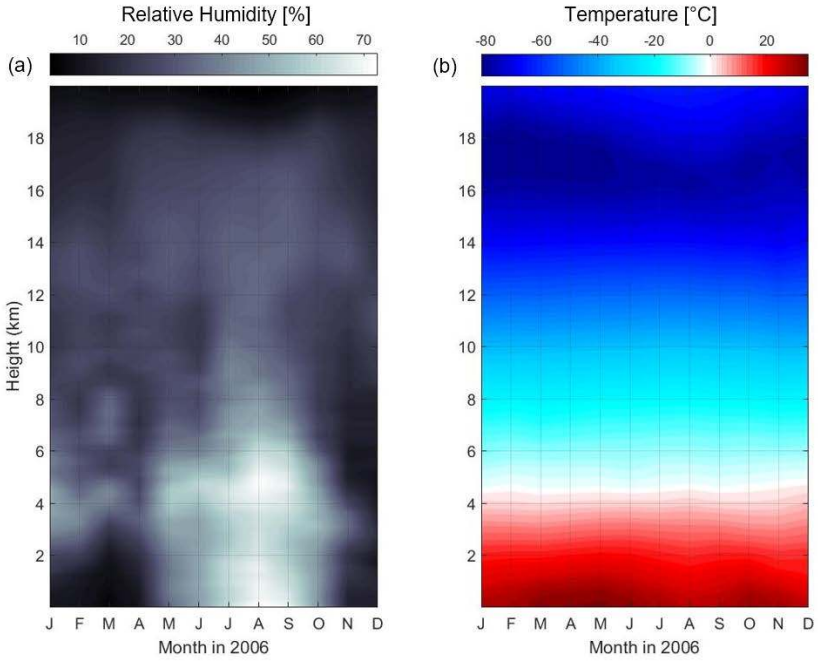

Fig. 4.3 Time-height cross sections of monthly-average (a) relative humidity and (b) temperature generated by combining in-situ measurements from radiosondes and radiometric retrievals from the microwave radiometer profiler at the AMF-1 site in Niamey, Niger during 2006.

Monthly-mean lifted-condensation level (LCL), convective available potential energy (CAPE), and convective inhibition (CIN) based on simple pseudo-adiabatic parcel theory (described in Appendix A) are shown in Fig. 4.1 (h), (i), and (k), respectively. The LCL is highest in March, then drops to half its maximum value by the start of the wet season, and reaches a minimum in August, coincident with the rainfall maximum. CAPE is unavailable throughout the dry season, then abruptly increases with the onset of the monsoon. On average CAPE increases at a slow, steady rate over the course of the monsoon season, starting at approximately 0.5 $kJ \cdot kg^{-1}$ in May and maximizing at 2.0 $kJ \cdot kg^{-1}$ near the end of September, before disappearing entirely at the end of October. Similar values of CAPE were found in this region by Monkam (2002) using low resolution thermodynamic profiles at mandatory levels. CIN is also not present during the dry season. Highest values of CIN occur at the onset of the wet season and decrease steadily to a peak season minimum.

4.2.4 Clouds

Cloud boundaries were determined at 42-meter resolution in the vertical every 6 seconds by combining data from the WACR, MPL, and CEIL as described in Kollias et al. (2009). Consistent with Miller et al. (2012) cloud area fraction is

defined as the fraction of each 1-hour period that clouds were present in the column. Monthly-mean cloud fractions are variable in the dry season, ranging 20 to 40%, and consistently higher at 60% throughout the length of the wet season (Fig. 4.1(k)). These values are consistent with the daily-mean cloud fraction derived from the SEVERI cloud mask (Slingo et al., 2009).

Monthly-mean liquid water path (LWP) and integrated water vapor (IWV) are shown in Fig. 4.1(l) and (m), respectively. Liquid water is nearly non-existent in the atmosphere over Niamey during the dry season. The LWP is elevated throughout the wet season, although the largest values are observed in June, July, and August of 2006. At the onset of the wet season, total column water vapor quickly doubles in comparison to its dry season presence, then slowly increases to a maximum coincident with the peak of the monsoon season, consistent with Miller et al. (2009).

4.2.3 The Surface Energy Balance

Surface fluxes of latent and sensible heat are shown in Fig. 4.1(n) and (o) respectively. The latent heat flux (LHF) remains below 10 $W \cdot m^{-2}$ for the duration of the dry season months, with a minimum value in May at the beginning of the wet season. During the wet season the LHF evolves in a manner similar to

accumulated monthly rainfall and CAPE, reaching a maximum in August at 60 W m^{-2}. The SHF evolves as near surface air temperatures, with maxima at the beginning and end of the wet season.

Surface downward shortwave radiative fluxes for all-sky and clear-sky conditions are presented in Fig. 4.1(p) and (q), respectively. Clear-sky conditions were identified using the technique described in Collow et al. (2015). Clear-sky fluxes peak early in the year, just before cloud cover returns to the Sahel at the start of the monsoon season then steadily declines until the beginning of the dry season in November. All-sky fluxes exhibit a similar range of variability although the decline over the course of the monsoon season is at first slower than that of the clear-sky fluxes, but more abrupt at the end. Surface downward longwave radiative fluxes for all-sky and clear-sky conditions are shown in Fig. 4.1(r) and (s), respectively. These fluxes are largest during the wet season, reflecting the seasonal cycles of cloud cover and integrated water vapor shown in Fig. 4.1(k) and (l), respectively.

Surface upward longwave radiative flux is presented in Fig. 4.1(t). This flux exhibits a maximum value in May that is coincident with the maximum in near surface air temperature shown in Fig. 4.1(b).

Chapter 5: Observation and Model Comparison

GCM performance may be assessed under the expectation that the seasonal cycle of any given quantity observed during a single year should be contained within the model-generated envelope of solutions for a decadal period that includes the year of observation (Miller et al., 2012). In the following, monthly-mean atmospheric fields for the single column of grid cells over Niamey, Niger was extracted from the first 10 years (2006 – 2015) of the RCP4.5 emissions scenario dataset for two CMIP5 coupled GCMs and compared to the observations of rainfall, meteorology, clouds, and radiation measured during 2006 in Niamey, Niger presented in Chapter 3. Model performance is then assessed in terms of the capability of each model to: 1) comprehensively capture 2006 monsoon cycle as characterized by the evolution various atmospheric quantities over the course of the year, 2) reproduce observed relationships between of such quantities and monthly accumulated rainfall.

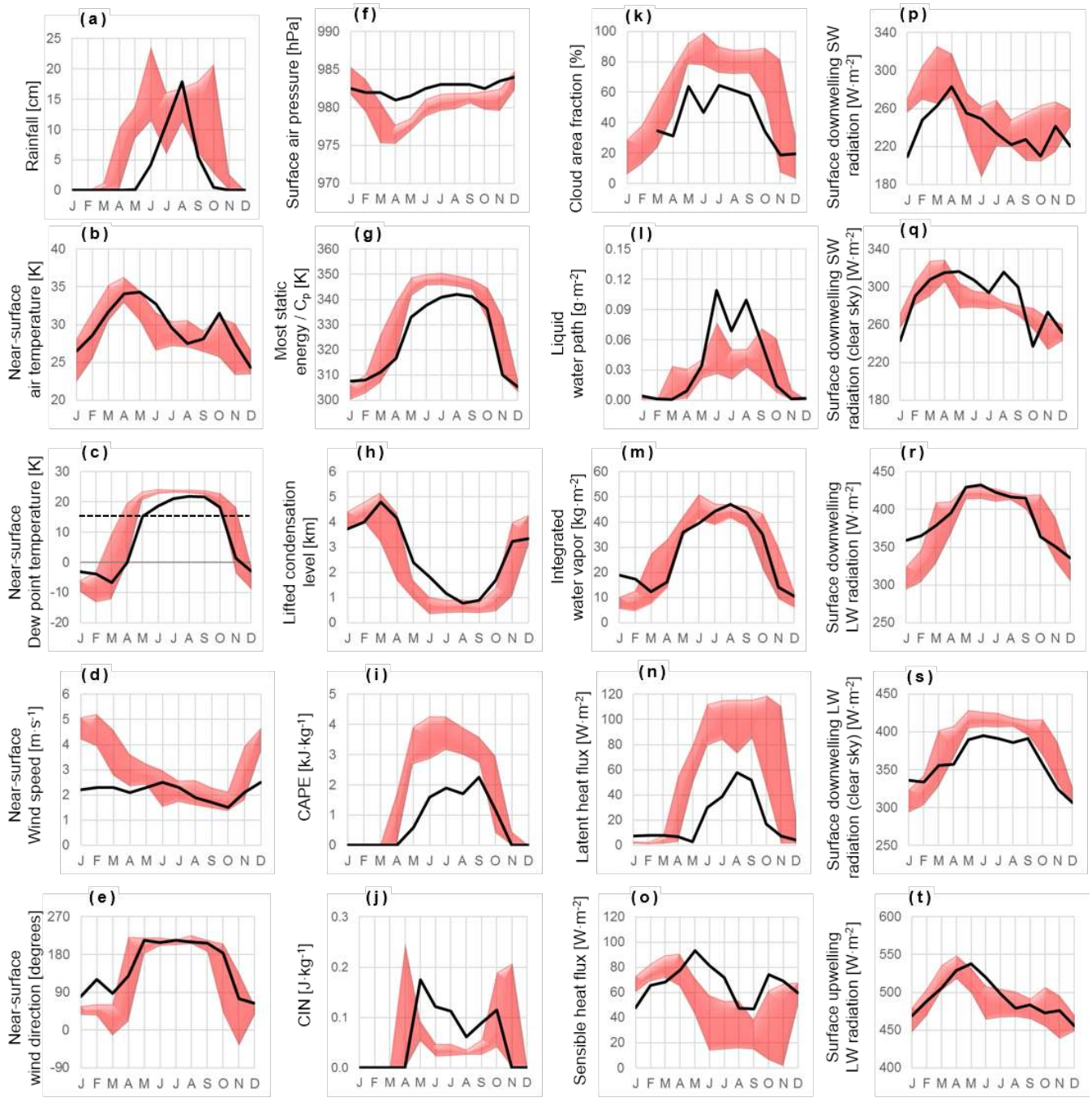

Fig 5.1 Same as Fig. 3.1 with the envelope of minimum and maximum monthly quantities simulated by GFDL-CM3 for 2006 – 2015.

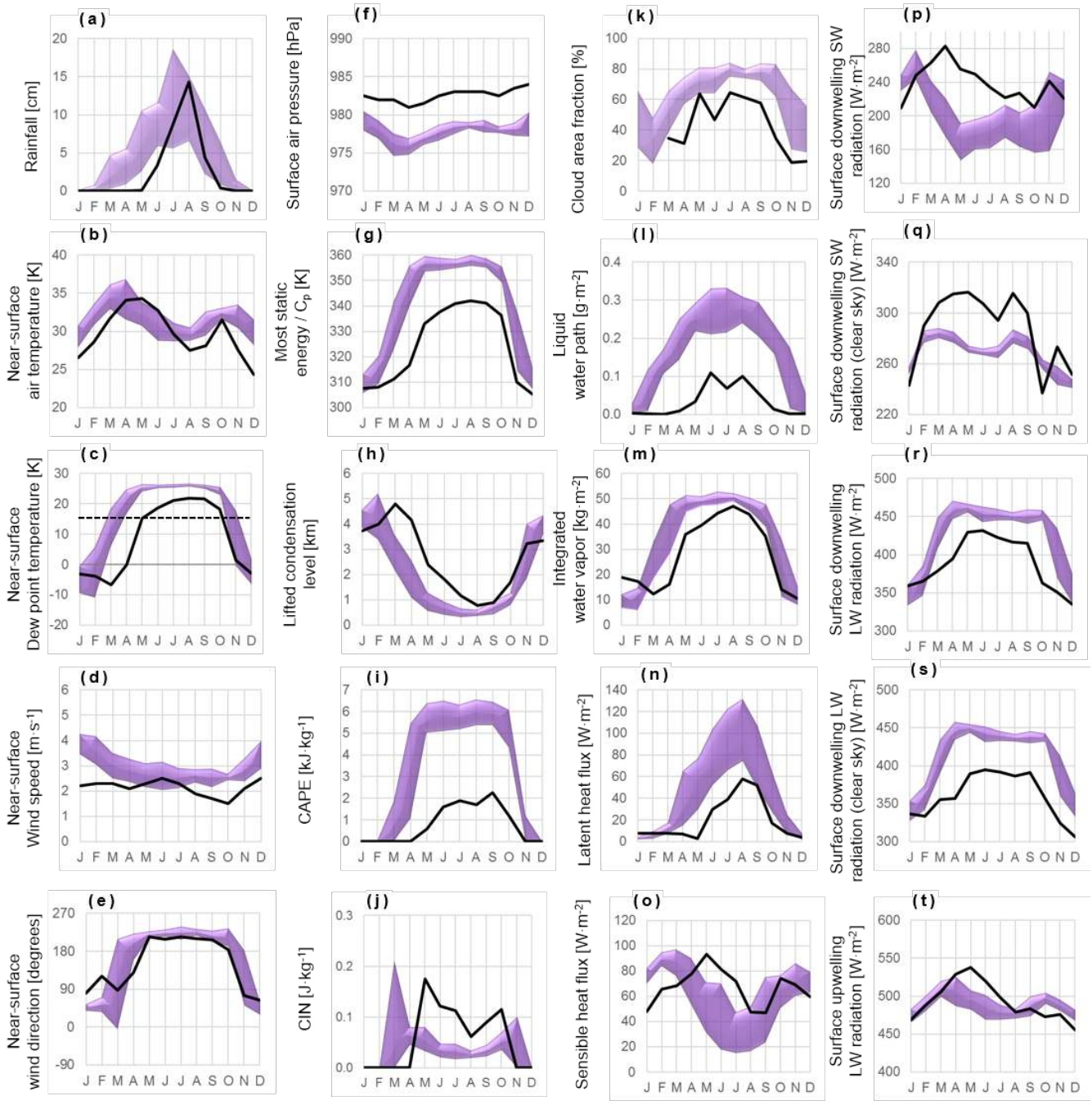

Fig. 5.2 Same as Fig. 3.1 with the envelope of minimum and maximum monthly quantities simulated by GISS-E2-R for 2006 – 2015.

5.1 Seasonal Cycles

The 2006 – 2015 envelope of seasonal cycles of rainfall, meteorology, the thermodynamic environment, clouds, and radiation from generated by GFDL-CM3 and GISS-E2-R for the RCP4.5 emissions scenario are compared to the seasonal cycles observed during 2006 in Niamey in Fig. 5.1 and Fig. 5.2 respectively.

5.1.1 Rainfall

Both models consistently simulate a seasonal rainfall cycle that is centered on, but extended beyond the observed wet season. GFDL-CM3 generally overestimates total annual rainfall (64 – 90 cm/year), and the peak rainfall month tends to occur either too early (as early as May) or too late (as late as October). The timing and magnitude of the observed annual cycle is better captured by GISS-E2-R, which simulates peak rainfall in July or August, and produces annual rainfall total ranging 42 – 67 cm/year. Rainfall that occurs too early (during February and March) or too late (during November and December) in GISS-E2-R simulations does not make a significant contribution to the simulated annual rainfall totals.

Simulated monthly rainfall totals were also extracted for the eight surrounding grid cells to ensure that spatial displacement was not a significant

source of error in the cycles simulated by either model. These results are provided in Appendix C.

5.1.2 Surface Meteorology

GFDL-CM3 captures the evolution of near-surface air temperature throughout the year (Fig. 4.1(b)), while GISS-E2-R simulates the basic evolutionary structure although temperatures are too high during the dry season, and peak one month earlier than observed (Fig. 5.2(b)). Both models simulate a generally appropriate range of near-surface dew point temperatures throughout the year (Fig. 5.1(c) & Fig. 5.2(c)), however both models simulate the onset of the monsoon season too early, as indicated by the occurrence of dew point temperatures above 15°C. Both models also fail to simulate the observed increase in dew point temperature over the course of the wet season.

Both models simulate a seasonal cycle of near-surface wind speeds that was not evident in the observations (Fig. 5.1(d) & Fig. 5.2(d)). While measurements during 2006 show little variation in near-surface wind speeds throughout the year, the models produce high wind speeds during the dry season that slowly decrease over the course of the wet season. Although this cycle is more pronounced in GFDL-CM3 than in GISS-E2-R, wind speeds observed during the wet season are

captured by the GFDL-CM3 decadal envelope, wind speeds simulated by GISS-E2-R are consistently higher than observed throughout the year. The observed shift in wind direction that is characteristic of the monsoon season is captured by GFDL-CM3 (Fig. 5.1(e)), however wind direction shifts 1 – 2 months earlier in GISS-E2-R than observed (Fig. 5.2(e)).

Both models exhibit deficiencies simulating the observed surface air pressure. GFDL-CM3 simulates a seasonal cycle with a minimum in pressure near the end of the dry season (Fig. 5.1(f)). GISS-E2-R simulates lower than observed pressure throughout the season but evolves with little variation as observed (Fig. 5.2(f)).

Although both models simulate the observed sharp increase in surface moist static energy at the start of the wet season, both overestimate the increase and fail to capture the steady increase in moist static energy over the course of the wet season (Fig. 5.1(g) and Fig. 5.2(g)).

5.1.3 The Thermodynamic Environment

Simulated seasonal cycles of the LCL, CAPE, and CIN were derived from vertical profiles output by each model at standard pressure levels using the same algorithm applied to the observations. Both models capture the magnitude and general

evolution of the LCL, although the reduction in LCL at the beginning of the wet season occurs too early in GISS-E2-R (Fig. 5.2(h)) and too rapidly in GFDL-CM3.

5.1.4 Clouds

Both models capture the seasonal cycle of cloud cover, but with about 10-20% too much cloud cover during the wet season. Although GFDL-CM3 (Fig. 5.1(k)) produces higher wet season cloud cover amounts (80-100% in June), it captures the 2006 dry season cloud amount. GISS-E2-R (Fig. 5.2(k)) produces too many clouds throughout the year, but produces more realistic cloud amounts during the wet season than GFSL, in comparison to the 2006 observations.

The models each simulate a seasonal cycle for the liquid water path (LWP) the peaks during the wet season, but these cycles are rather different in terms of magnitude and evolution. GFSL-CM3 (Fig. 5.1(l)) produces LWP values that capture the 2006 observations during the dry season, but too low from June through September. GISS-E2-R (Fig. 5.2(l)) simulates the LWP with values that are nearly three times larger than observed throughout the year. Despite these differences, both models capture the 2006 seasonal cycle of total column water vapor rather well. GFDL-CM3 produces values that closely represent the 2006 observations in all months with the exception of January (Fig. 5.1(m)). GISS-E2-

R envelope is slightly higher than the 2006 observation, during the first half of the year, but still captures the evolution of total column water vapor (Fig. 5.2(m)).

5.1.5 The Surface Energy Balance

The LHF is over estimated during the wet season in both models, however, the observed evolution of the LHF over the course of the first half of the 2006 wet season (May – August) is more closely resembled by GISS-E2-R (Fig. 5.2(n)) than by GFDL-CM3 (Fig. 5.1(n)), which simulates an abrupt increase in the LHF to peak season values at the beginning of the monsoon season in June. Both models capture a seasonal cycle for the SHF similar to the 2006 observations, but the observed May maximum and August-September minimum are each produced about 2 months early by both models (Fig. 5.1(o) & Fig. 5.2(o)).

GFDL-CM3 captures the evolution and magnitude of the observed 2006 seasonal cycles of surface radiative fluxes extraordinarily well (Fig. 5.1(p) – (t)). GISS-E2-R produces comparable seasonal evolution but simulates low amounts of surface downwelling SW radiation for both all-sky and clear-sky conditions, and simulates large values of surface downwelling longwave radiation for both clear-sky and all-sky conditions throughout the year (Fig. 5.2 (p) – (t)).

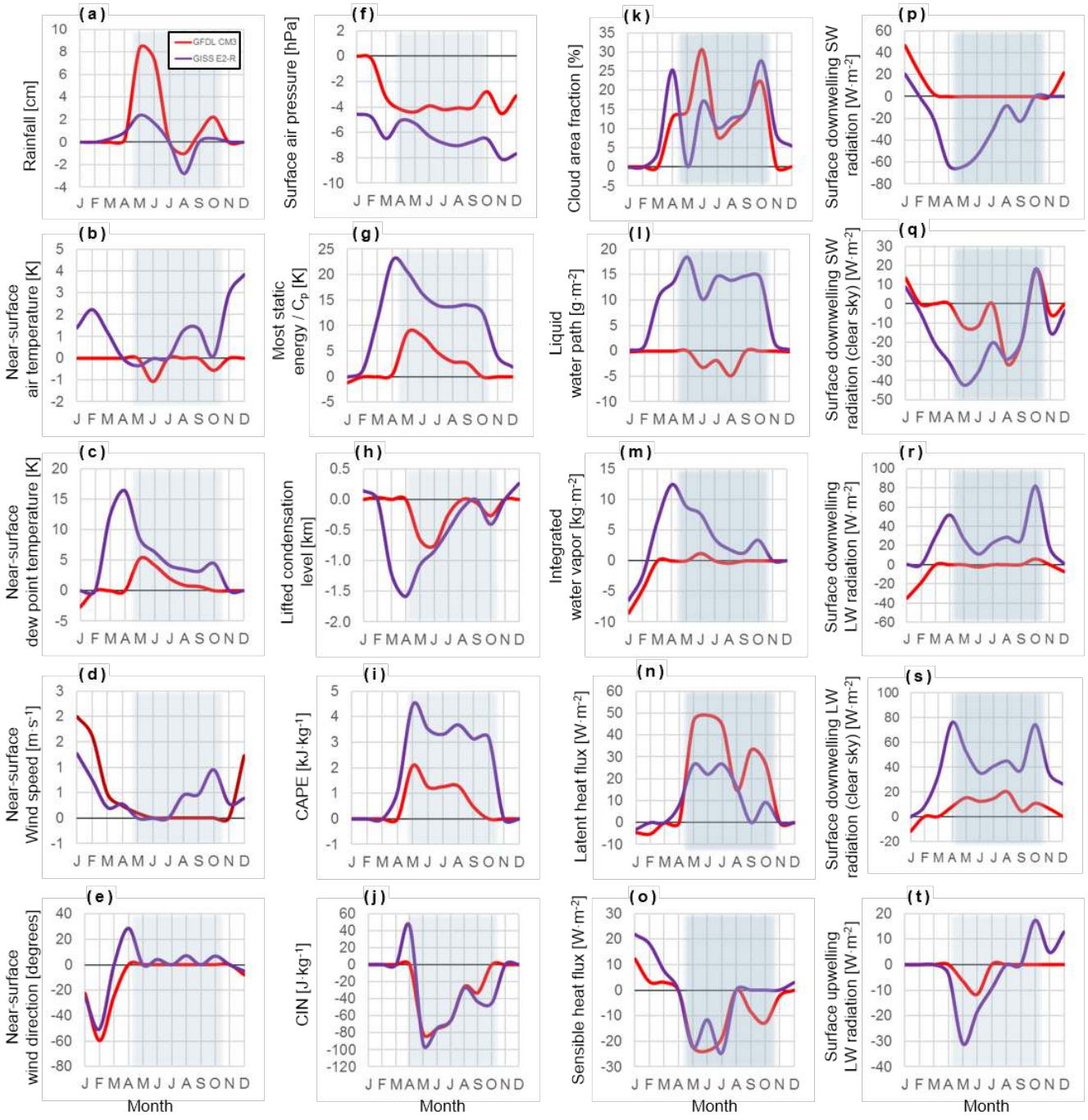

Fig. 5.3 Comparison of time series of monthly-mean errors in the same quantities as Fig. 3.1 simulated by GFDL-CM3 (red) and GISS-E2-R (purple). Errors are nonzero for months when the 2006 observed value is not captured within the range of 2006 – 2010 simulated values for a particular model, and defined as the difference between the observed 2006 value and the upper or lower boundary of the simulated decadal envelope.

5.2 Model Intercomparison

5.2.1 Errors in Seasonal Cycles

For any given simulated variable, model error is quantified for each calendar month as the magnitude of the difference between the value observed during such month in 2006 and the nearest bound of the decadal envelope simulated by the model. For months in which a model captures the 2006 seasonal cycle within its decadal envelope, the model error is defined as zero. Errors corresponding to the decadal envelopes simulated by GFDL-CM3 and GISS-E2-R are directly compared in Fig. 5.3

With regards to the capability of the models to capture the 2006 monsoon season, GFDL-CM3 is superior to GISS-E2-R for all evaluated quantities with a few notable exceptions. The models have roughly equal magnitudes of error with respect to cloud fraction (Fig. 5.3(k)) and sensible heat flux (Fig. 5.3(o)). GISS-E2-R has substantially less error than GFDL-CM3 for rainfall (Fig. 5.3(a)) and latent heat flux (Fig. 5.3(n)). While the model errors frequently differ in terms of magnitude, they follow remarkably similar trends over the course of the year. Errors tend to be largest, especially for the GISS-E2-R model, during the transition

from the dry season to the wet season in March, April, and May. The larger magnitudes of error during this time period indicates that the elevated early-season rainfall in GISS-E2-R is consistent with an early onset of the monsoon reflected by other simulated quantities (e.g., near surface dew point temperature, wind speeds, and the LCL).

Following the same method applied above to 2-D atmospheric fields, errors in simulated monthly-average vertical profiles of temperature and specific humidity were computed against observed profiles interpolated to the standard pressure levels available in the model output (Fig. 5.4). For GISS-E2-R, temperature errors are minimum in the lower atmosphere, but too cool by 2-3 °C between 9 and 12 km during the peak monsoon season. Temperature errors are largest for this model in the upper atmosphere (but within ±5 °C). Most apparent are warm errors between 14 and 18 km during January through May, and cool errors near 18 km during the core of the monsoon season, from June through September. GISS-E2-R simulates an excess of humidity below 3 km that is most pronounced during early monsoon season months from April – June with magnitudes near 5 $g \cdot kg^{-1}$. GFDL-CM3 presents a rather striking capability to simulate the thermodynamic environment throughout the entire seasonal cycle. Temperatures are slightly cool

(less than 1 °C) for nearly the entire depth of the atmosphere during monsoon months. Errors in specific humidity for GFDL-CM3 only appear in January (too dry by about 2 $g \cdot kg^{-1}$) near 3 km, and in June (too wet by about 2 $g \cdot kg^{-1}$) at the surface.

Although GFDL-CM3 captures the seasonal evolution of these variables with less error than GISS-E2-R, its relatively poor simulation of early-season rainfall indicates a possible disconnect in the subgrid-scale physics. Whether or not GFDL-CM3's simulation of the west African monsoon is less coordinated than that of GISS-E2-R is further explored in the next section.

5.2.2 Correlations

To further quantify model performance, time series of monthly accumulated rainfall simulated by each model over the decade from 2006 – 2015 were correlated with all other quantities individually (Fig. 5.5). Correlation coefficients characterizing the relationship between rainfall and all other quantities were evaluated against correlation coefficients determined from the observations in 2006 (Table 5.1).

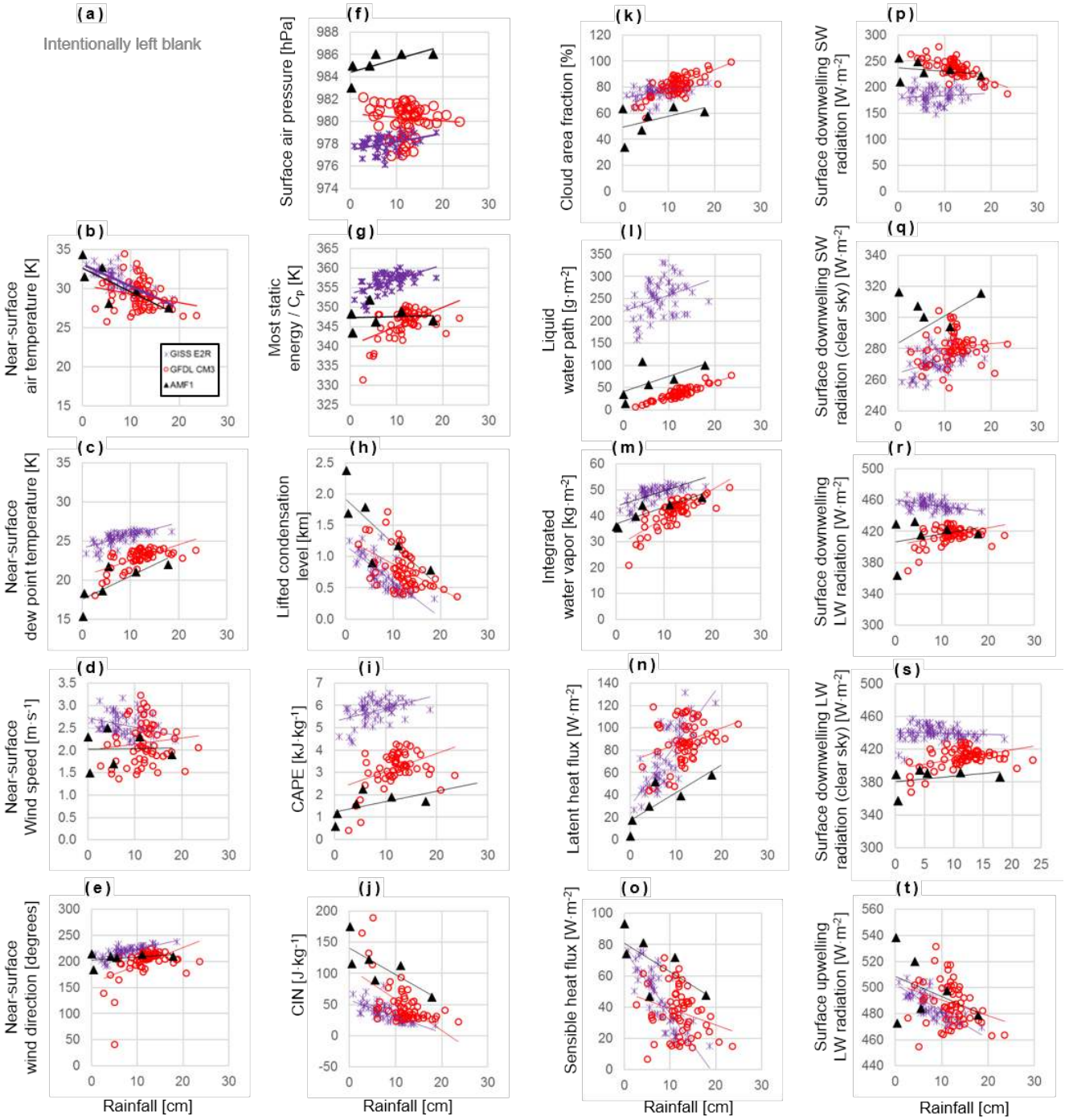

Fig. 5.5 Monthly-mean values for the quantities in Fig. 3.1 versus monthly-mean precipitation as observed by the AMF-1 in 2006 (black triangles) and as simulated during 2006 – 2010 by GISS-E2-R (purple asterisks) and GFDL-CM2 (red open circles). A linear fit to the monthly-means is indicated by solid lines of corresponding color. The value of R^2 reflecting the amount of variance explained by each fit is listed in Table 4.2 for each quantity.

Table 5.1 Correlation coefficients corresponding to the linear relationships between monthly accumulated rainfall total and other atmospheric quantities determined from the scatterplots presented in Fig. 4.5.

Variable	AMF-1	GFDL-CM3	GISS-E2-R
Rainfall	1.00	1.00	1.00
Near-surface air temperature	0.61	0.10	0.60
Near-surface dew point temperature	0.61	0.49	0.46
Near-surface winds speed	0.00	0.01	0.17
Near-surface wind direction	0.14	0.28	0.46
Surface air pressure	0.48	0.01	0.29
Moist Static Energy/Cp	0.00	0.43	0.43
Lifting condensation level	0.63	0.34	0.60
CAPE	0.30	0.34	0.36
CIN	0.59	0.45	0.55
Cloud fraction	0.24	0.49	0.36
Liquid water path	0.43	0.84	0.28
Integrated water vapor	0.84	0.69	0.53
Latent heat flux	0.67	0.25	0.71
Sensible heat flux	0.45	0.13	0.72
Surface downwelling shortwave radiation	0.07	0.40	0.01
Surface downwelling shortwave radiation (clear-sky)	0.16	0.03	0.05
Surface downwelling longwave radiation	0.07	0.25	0.03
Surface downwelling longwave radiation (clear-sky)	0.10	0.19	0.01
Surface upwelling longwave radiation	0.17	0.12	0.60

Six different quantities were observed to have strong relationships with precipitation during the 2006 wet season: near-surface air temperature, near-surface dew point temperature, the LCL, CIN, integrated water vapor and latent heat flux (Fig. 5.5(b), (c), (h), (j), (m) and (n), respectively). GISS-E2-R simulations show similarly strong correlations for each of these variables with the exception of dew point tempzerature, for which the correlation is slightly weaker. GFDL-CM3

simulations reproduce a strong correlation between precipitation and integrated water vapor, but reproduce weak correlations with respect to the near-surface dew point temperature, LCL, CIN and LHF, and essentially no relationship between precipitation and near-surface air temperature.

Surface air pressure, CAPE, cloud fraction, LWP, and sensible heat flux were observed to correlate weakly with precipitation in 2006 (Fig. 5.5(f), (i), (k), (l), and (o), respectively). GISS-E2-R reproduces similarly weak correlations for each of these quantities, with the exception of the sensible heat flux, which exhibits a strong relationship with simulated precipitation. GFDL-CM3 simulations show weak relationships with respect to cloud fraction and CAPE that are similar to the observed. However, GFDL-CM3 reproduces a strong correlation with respect to the LWP, and essentially no correlation with respect to surface air pressure and the sensible heat flux.

Observations during 2006 revealed little or no relationships between the seasonal cycle of precipitation and wind speed, wind direction, moist static energy, or any of the surface radiative fluxes (Fig. 5.5(d), (e), (g), (p)-(t), respectively.) GISS-E2-R simulations show similarly weak correlations for near-surface wind speed, downward shortwave radiation at the surface for all-sky and clear-sky, and

downward longwave radiation at the surface. Wind direction and moist static energy exhibit weak correlations in GISS-E2-R simulations, and a uniquely strong correlation is shown with respect to upward longwave radiation at the surface. GFDL-CM3 reproduces the observed weak correlations between precipitation and wind speed, downward shortwave radiation at the surface for clear-sky conditions, and upward longwave radiation at the surface. Weak correlations are found with respect to wind direction, moist static energy, downward shortwave radiation at the surface (all-sky) and downward longwave radiation at the surface.

On the basis of these results, the originating sources of error with respect to the simulation of rainfall appear to be unique to each model. Simulations from GISS-E2-R reproduced relationships between precipitation and nearly all evaluated quantities that were remarkably similar to those observed during 2006. The fact that the evolution of rainfall is largely consistent with the evolution of other atmospheric fields suggests that the treatment of convective rainfall in this model does not contain deficiencies that significantly influence model performance on seasonal time scales. The tendency to of this model to simulate the start of the monsoon season early is then most likely rooted in non-local sources of error. GFDL-CM3 captures the 2006 seasonal cycles for nearly all evaluated quantities,

yet does not reproduce the observed relationships between the evolution of rainfall and all other quantities. The dominant source of error in this model appears to come from deficiencies in the treatment of convective rainfall.

Chapter 6: Connecting Subgrid-Scale Physics with Grid-Scale Performance

6.1 Discussion

The persistent lack of agreement in projections of rainfall in the Sahel among different GCMs has been generally attributed to challenges associated with the representation of convective processes. To establish the degree to which convective parameterizations may influence seasonal-scale model output more definitively, a single column of standard model output was extracted from the CMIP5 dataset for two GCMs and compared with the observed seasonal evolution of rainfall, surface meteorology, the thermodynamic state of the atmosphere, clouds and radiation, obtained during the RADAGAST experiment in Niamey, Niger. This approach enables a unique comprehensive assessment of seasonal rainfall simulations and provides valuable insight into how the parameterization of convective processes relate to model performance on seasonal scales that could not be gained from traditional model evaluations techniques. It was found that local sources of error

originating from the representation of subgrid-scale convective processes may significantly impact simulations of the seasonal cycle of rainfall in some models. Based on the relative performance of each model in combination with their respective formulations, a physically-based treatment of convective rainfall may be critical to successful simulation of rainfall on seasonal time scales.

Some additional findings deserve specific mention. First, both models demonstrated a remarkable overall capability to simulate the set of variables representing the seasonal cycles of surface meteorology, the thermodynamic environment, clouds and radiation that characterize the WAM. A less comprehensive study that uses JAS rainfall totals as a reflection of the capability of GCMs to simulate convection may not reach the same conclusion. As demonstrated by the performance of GFDL-CM3 in this study, low JAS rainfall may result from errors in timing of peak-season rainfall, not the inability of the model to simulate a monsoon season. As also demonstrated by GFDL-CM3, errors in timing may simply be a reflection of the model's handling of convection precipitation, and does not speak for its ability to simulate other aspects of convection. These considerations shed a different light the capability of GCMs to

simulate the WAM and allow for the possibility that progress simulating convection in this region may be understated.

The availability of only a single year of observations in Niamey is a significant limitation with two major implications for the present study. First, the observed correlation coefficients that quantify the relationships between rainfall and all other quantities are less robust than those computed for the simulations, which were determined from 10 years of data. Second, it is not possible to evaluate the year-to-year variability in the simulated seasonal cycles, which could have illuminated additional errors that were otherwise not identified by this study. These limitations, however, should not overshadow the fact that the RADAGAST dataset represents a rare wealth of observations that may not be available in the Sahel again for some time.

The uniformity of the landscape in the Sahel is a major factor that allows for the comparison of grid-cell average quantities to point observations as done so in this study. Successful application of this method to other regions with similar available datasets from other AMF-1 deployments is not immediately obvious. Additional research would most likely be required to show that monthly-average observations are comparable to model output in other locations. How applicable

the results of the present study are to the rest of the Sahel is unclear. Further study is required to determine how local and non-local sources of error may vary in relation to each other within a given region.

Despite the above-mentioned limitations, the analysis defined by the scope of this study hardly exhausted the utility of the evaluation dataset. Specifically, further evaluation could have been performed by comparing simulated and observed relationships between all possible combinations of quantities. Such results may be useful to study the influence of the models' formulations of convective processes other than rainfall on seasonal-scale performance. The results of this study might also be especially useful for interpretation of the future rainfall projections for the emissions scenario dataset that was utilized in the present-day evaluation. GCM capabilities to reproduce the present-day climate are typically limited to a historical time period that precedes the start of emission scenario projections. The fact that the simulations used in this study to represent the present-day climate were extracted from the first decade of data available for RCP4.5 makes the results of the evaluation slightly more relevant for the interpretation of future rainfall projections in the Sahel.

6.2 Conclusions

This study confirms that deficiencies in subgrid-scale physics can be a significant source of error in GCM simulations of rainfall at seasonal scales and, in some models dominate non-local sources of error. While deficiencies in subgrid-scale physics are unique to each model's formulation, the capability to simulate the seasonal cycle of rainfall in the Sahel appears to be more sensitive to a realistic representation of convective precipitation microphysics than to a realistic representation of the organization of convective structures. Information characterizing the nature of errors in rainfall simulations at seasonal scales such as this can be a valuable supplement to model evaluations performed using traditional methods and ultimately help expedite the resolution of long-standing issues with GCM simulations in the Sahel.

Increasing the certainty in GCM projections of rainfall in the Sahel is but one of many important challenges that model developers continue to be faced with. Given these challenges, an effort to increase the efficiency of the model development process is a task of equal importance to development efforts in and of themselves. Although this study sheds light on the enormity of the task at hand, it also illuminates a path by which the larger scientific community can contribute to an

increased understanding of model performance, given knowledge of how GCMs are formulated.

The sensitivity of seasonal-scale GCM performance in the Sahel to the microphysical treatment of convective precipitation in the model's formulation provokes further exploration into the mechanisms of communication between the land surface and the atmosphere in this region. Future work should answer key questions regarding the relevance of these microphysical communications to the evolution of rainfall within a given season and how these communications may be effected in future climate change scenarios. Such knowledge would be invaluable not only for the Sahel, but for any other region that depends so critically on its local agriculture.

Appendix A: Computation of CAPE and CIN

The following describes the methodology used to approximate CAPE and CIN based on the ascent of a mixed-layer parcel using simple, psuedoadiabatic pure parcel theory. The MS_{ecmwf} and MS_{mwrp} high-resolution data products provide temperature T_c in °C, relative humidity, RH in %, and barometric pressure, P in mb, for 266 levels from the surface (level 0) to a height of 20 km (level 266).

Physical constants used in this formulation were defined as follows: Gas constant for dry air, $R_d = 287.04\ \mathrm{J \cdot kg^{-1} \cdot K^{-1}}$, gas constant for water vapor, $R_v = 461.50\ \mathrm{J \cdot kg^{-1} \cdot K^{-1}}$, specific heat of dry air at constant pressure, $C_{pd} = 1005.7\ \mathrm{J \cdot kg^{-1} \cdot K^{-1}}$, specific heat of water vapor at constant pressure, $C_{pv} = 1875\ \mathrm{J \cdot kg^{-1} \cdot K^{-1}}$, acceleration due to gravity, $g = 9.81\ \mathrm{m \cdot s^{-2}}$. Meteorological variables, including absolute temperature, potential temperature, virtual temperature, vapor pressure, and water vapor mixing ratio were computed using the relationships and empirical formulas of Bolton [1980].

The initial parcel assumes the average properties of the environment (mixing ratio and potential temperature) within and including level 2 through level 8, at the pressure (and height) of level 5, as determined for each individual sounding. The lifted condensation level (LCL) temperature and height, and pseudoequivalent potential temperature are approximated from the temperature, pressure, height and vapor pressure of the initial parcel as follows:

LCL temperature [Bolton, 1980]:

$$T_{LCL} = \frac{2840}{3.5\ln T - \ln e - 4.805} + 55 \tag{A1}$$

LCL height [Emanuel, 1994]:

$$z_{LCL} = z + \left(\frac{C_{pd}}{g}\right)\frac{1+\frac{rC_{pv}}{C_{pd}}}{1+r}\left(T - T_{LCL}\right) \tag{A2}$$

Pseudoequivalent potential temperature [Bolton, 1980]:

$$\theta_{ep} = T\left(\frac{1000}{P}\right)^{0.2854(1-0.28r)} \exp\left[r(1+0.81r)\frac{3376}{T_{LCL} - 2.54}\right] \tag{A3}$$

The temperature of the parcel is determined at each vertical level by raising the parcel dry adiabatically below the LCL height, and pseudoadiabatically according to (B3) above the LCL height. (B3) was solved numerically according

to the method described in Stackpole (1967). The buoyancy of the parcel relative to the environment as described by the model sounding was then determined for each model level as follows:

$$B = \frac{T_{v,par} - T_{v,env}}{T_{v,env}} \tag{A4}$$

The level of free convection (LFC) virtual temperature and height were linearly interpolated from the temperature and height of the lowest model level above the LCL with positive buoyancy and that of the immediately preceding, negatively buoyant level. For cases in which the first model level above the LCL is positively buoyant, the LFC temperature and height are set equal to that of the LCL. The equilibrium level (EL) temperature and height were linearly interpolated from the temperature and height of the lowest model level above the LFC with negative buoyancy and that of the immediately preceding, positively buoyant level.

For each layer between level five and the EL, the mean-layer potential energy (MLPE) is computed as follows:

$$MLPE = \frac{B_i - B_{i+1}}{2} g\left(z_{i+1} - z_i\right) \tag{A5}$$

For layers in which buoyancy changes sign (i.e., LFC and EL layers), the MLPE is calculated separately for the portions of each layer above and below the LFC and EL. The upper level potential energy (ULPE) and lower level potential energy (LLPE) for the LFC and EL layers is defined as:

$$ULPE = \frac{B_{i+1}}{2} g\left(z_{i+1} - z\right) \tag{A6}$$

$$LLPE = \frac{B_i}{2} g\left(z - z_i\right) \tag{A7}$$

CIN is determined from the MLPE of each layer from level 5 to the layer immediately below the LFC, and the LLPE of the layer that includes the LFC. CAPE is determined from the ULPE of the layer that includes the LFC, the MLPE of each layer from the layers between the LFC and EL, and the LLPE of the layer that includes the EL. In the event that no LFC exists in a given profile, CAPE and CIN are accordingly undefined.

Appendix B: Uncertainty equations for cloud microphysical properties

Cloud Water Phase Partition

The following simple mixed-mode fractionating scheme based on MS_{ecmwf} high-resolution temperature profiles is used to determine ice fraction i and liquid water fraction ℓ which separate the total measured radar reflectivity factor Z_T [$mm^6\ m^{-3}$] into ice and liquid water portions (Z_i and Z_ℓ, respectively) for temperatures between -16 and 0°C :

$$i = -T/16$$

$$\ell = 1 - i = 1 + T/16$$

$$Z_i = iZ_T = -\frac{T}{16}Z_T$$

$$Z_\ell = \ell Z_T = \left(1 + \frac{T}{16}\right)Z_T$$

Ice Water Content

Ice water content (IWC) is determined from Z_i by the empirical relationship of Liu and Illingworth (2000):

$$\mathrm{IWC} = 0.097 Z_{\mathrm{i}}^{0.59} = 0.097 \left(-\frac{T}{16} Z_{\mathrm{T}}\right)^{0.59}$$

The uncertainty in IWC based on the uncertainty in temperature δT is given by:

$$\delta \mathrm{IWC} = \frac{d\mathrm{IWC}}{dT} \delta T = 0.097 \left(\frac{Z_T}{16}\right)^{0.59} \frac{d}{dT} (-T)^{0.59} \delta T = -0.05723 \frac{\left(\frac{Z_T}{16}\right)^{0.59}}{(-T)^{0.41}} \delta T$$

Ice Cloud Particle Effective Radius

Ice cloud particle effective radius (r_{ei}) is a function of temperature according to Ivanova et al. (2001):

$$r_{ei} = \frac{75.3 + 0.5895T}{2}$$

The uncertainty in r_{ei} based on the uncertainty in temperature δT is given by:

$$\delta r_{ei} = \frac{dr_{ei}}{dT} \delta T = \frac{d}{dT} \left[\frac{75.3 + 0.5895T}{2}\right] \delta T = 0.29475 \, \delta T$$

Liquid Water Content

Liquid water content (LWC) is based on Z_l and an assumed reference cloud particle number N_0 of 100 cm^{-3}, as derived by Liao and Sassen (1994):

$$\mathrm{LWC} = \left(\frac{N_0 Z_\ell}{3.6}\right)^{5/9} = \left[\frac{N_0\left(1+\frac{T}{16}\right)Z_\mathrm{T}}{3.6}\right]^{5/9}$$

The uncertainty in LWC based on the uncertainty in temperature δT is given by:

$$\delta\mathrm{LWC} = \frac{d\mathrm{LWC}}{dT}\delta T = \left(\frac{N_0 Z_\mathrm{T}}{3.6}\right)^{5/9}\frac{d}{dT}\left(1+\frac{T}{16}\right)^{5/9}\delta T = \frac{5\left(\frac{N_0 Z_\mathrm{T}}{3.6}\right)^{5/9}}{144\left(1+\frac{T}{16}\right)^{4/9}}\delta T$$

Liquid Water Effective Radius

Liquid water effective radius (r_e) is a function of the LWC, assuming a log-normal droplet distribution with a width $\sigma$of 0.35 and cloud particle number concentration N_d equal to 200 cm^{-3} according to Frisch et al. (1995):

$$r_e = 1.358\left[\frac{3\mathrm{LWC}}{4\pi\rho_w N_d \exp\left(\frac{9\sigma^2}{2}\right)}\right]^{1/3}$$

The uncertainty in r_e based on the uncertainty in temperature δT is given by:

$$\delta r_e = \frac{dr_e}{dT}\delta T = 1.358\frac{dr_m}{dT} = 1.358\frac{dr_m}{d\mathrm{LWC}}\frac{d\mathrm{LWC}}{dT}$$

$$\frac{dr_m}{d\mathrm{LWC}} = \frac{1}{3}\left[\frac{3}{4\pi\rho_w N_d \exp\left(\frac{9\sigma^2}{2}\right)}\right]^{1/3}$$

$$\mathrm{LWC}^{-2/3} = \frac{1}{3}\left[\frac{3}{4\pi\rho_w N_d \exp\left(\frac{9\sigma^2}{2}\right)}\right]^{1/3}\left[\frac{N_0\left(1+\frac{T}{16}\right)Z_\mathrm{T}}{3.6}\right]^{-10/27}$$

$$\delta r_e = \frac{1.358}{3}\left[\frac{3}{4\pi\rho_w N_d \exp\left(\frac{9\sigma^2}{2}\right)}\right]^{1/3}\left[\frac{N_0\left(1+\frac{T}{16}\right)Z_\mathrm{T}}{3.6}\right]^{-10/27}\left[\frac{5\left(\frac{N_0 Z_\mathrm{T}}{3.6}\right)^{5/9}}{144\left(1+\frac{T}{16}\right)^{4/9}}\right]\delta T$$

$$\delta r_e = \frac{6.79}{432}\left[\frac{3}{4\pi\rho_w N_d \exp\left(\frac{9\sigma^2}{2}\right)}\right]^{1/3}\frac{\left(\frac{N_0 Z_\mathrm{T}}{3.6}\right)^{5/27}}{\left(1+\frac{T}{16}\right)^{22/27}}\,\delta T$$

Appendix C: Simulated Seasonal Cycles of Rainfall in the Region Surrounding Niamey

The evolution of monthly-mean rainfall rate derived from measurements recorded by the AMF-1 PWD during 2006 in Niamey, Niger are compared to the 2006 – 2015 envelopes of minimum and maximum monthly-average rainfall rate simulated by GISS-E2-R for the grid cell containing Niamey (Fig. D.1-e) and the eight surrounding grid cells (Fig. D.1-a, b, c, d, f, g, h, i). Consistent with the spatial distribution of annual rainfall totals reported by Lélé and Lamb (2010), GISS-E2-R simulates higher monthly-average rainfall rates (indicating larger monthly accumulated rainfall totals) throughout the monsoon season to the south and east of the grid cell containing Niamey, while lower monthly-average rainfall rates are produced to the north and east of the grid cell containing Niamey. GFDL-CM3 produces a similar pattern of monthly-mean rainfall rates (Fig. D.2). It is therefore concluded that spatial displacement is not a significant source of error in the monthly average rainfall rates simulated by these two models for the grid cell including Niamey.

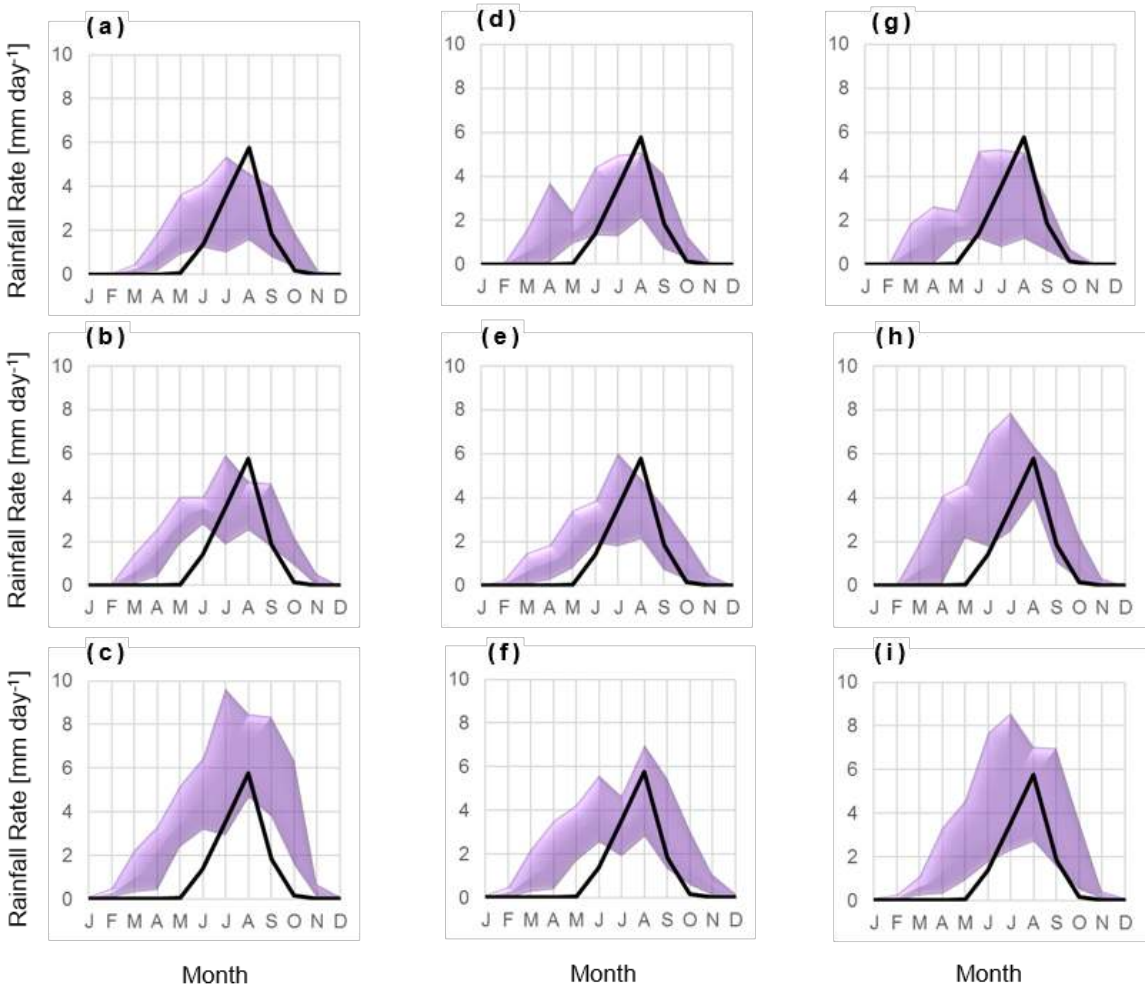

Fig. C.1 Envelopes of minimum and maximum monthly-mean rainfall rate simulated by GISS-E2-R in the grid cells (a) northwest, (b) west, (c) southwest, (d) north, (f) south, (g) northeast, (h) east, and (i) southeast of (e) the grid cell containing Niamey, Niger during the period 2006 – 2010 compared to the values derived from AMF-1 measurements during 2006 in Niamey, Niger.

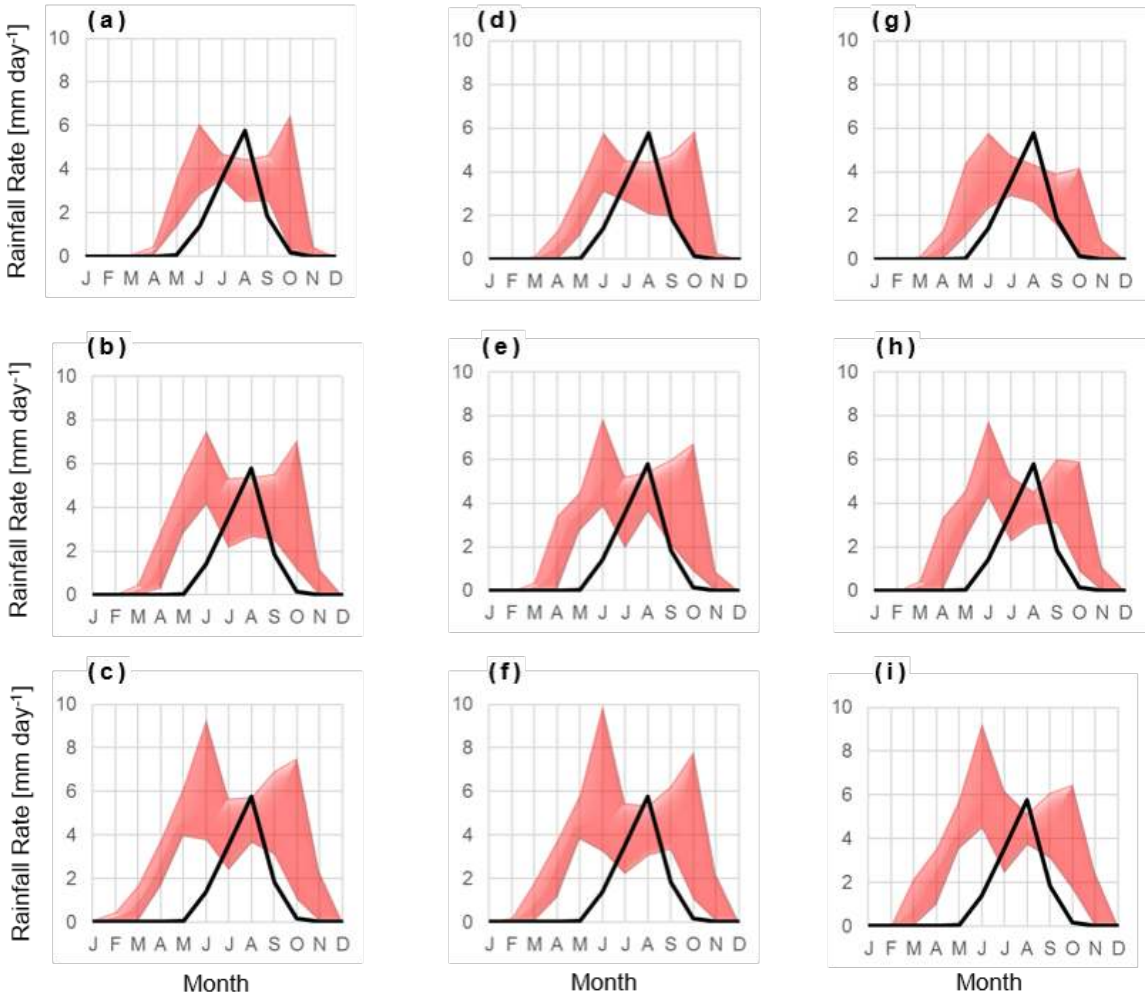

Fig. C.2 Same as Fig. C.1 except for GFDL-CM3.

References

Askne, J. I. H., and E. R. Westwater, 1986: A review of ground-based remote sensing of temperature and humidity by passive microwave radiometers. *IEEE Transactions on Geoscience and Remote Sensing*, **GE-24**, 340-352.

Augustine, J.A., J.J. DeLuisi, and C.N. Long, 2000: SURFRAD – A national surface radiation budget network for atmospheric research. *Bull. Amer. Meteor. Soc.* **133**, 1993-2010.

Biasutti, M., I. M. Held, A. H. Sobel, and A. Giannini, 2008: SST forcings and Sahel rainfall variability in simulations of the twentieth and twenty-first centuries. J. Climate, 21, 3471– 3486.

Bolton, D., 1980: The computation of equivalent potential temperature. *Mon. Wea. Rev.*, **108**, 1046-1053.

Bony, S., and J-L. Dufresne, 2005: Marine boundary layer clouds at the heart of tropical cloud feedback uncertainties in climate models. *Geophys. Res. Lett.*, **32**, L20806.

Cadeddu, M. P., J. C. Liljegren, and D. D. Turner, 2013: The atmospheric radiation measurement (ARM) program network of microwave radiometers: instrumentation, data, and retrievals. *Atmos. Meas. Tech.*, **6**, 2359-2372.

Christensen, J.H., K. Krishna Kumar, E. Aldrian, S.-I. An, I.F.A. Cavalcanti, M. de Castro, W. Dong, P. Goswami, A. Hall, J.K. Kanyanga, A. Kitoh, J. Kossin, N.-C. Lau, J. Renwick, D.B. Stephenson, S.-P. Xie and T. Zhou, 2013: Climate

Phenomena and their Relevance for Future Regional Climate Change. In: Climate Change 2013: The Physical Science Basis. Contribution of Working Group I to the Fifth Assessment Report of the Intergovernmental Panel on Climate Change [Stocker, T.F., D. Qin, G.-K. Plattner, M. Tignor, S.K. Allen, J. Boschung, A. Nauels, Y. Xia, V. Bex and P.M. Midgley (eds.)]. Cambridge University Press, Cambridge, United Kingdom and New York, NY, USA, pp. 1217–1308, doi: 10.1017/CBO9781107415324.028.

Cimini, D., T. Hewison, L. Martin, J. Güldner, C. Gaffard, and F. Marzano, 2006: Temperature and humidity profile retrievals from ground-based microwave radiometers during TUC. *Meteor. Z.*, **15**, 45-56, doi:10.1127/0941-2948/2006/0099.

Collow, A. B., Ghate, V. P., Miller, M. A. and Trabachino, L. C. (2016), A one-year study of the diurnal cycle of meteorology, clouds and radiation in the West African Sahel region. Q.J.R. Meteorol. Soc., 142: 16–29. doi: 10.1002/qj.2623

Cook, K.H., and E.K. Vizy, 2006: Coupled model simulations of the West African monsoon system: Twentieth- and twenty-first century simulations. *J. Climate*, **19**, 3681 – 3703.

Cook, D.R. and M.S. Pekour, 2008: Eddy correlation flux measurement system handbook. *Tech. Rep. DOE/SC-ARM/TR-05I,* Off. of Biol. and Environ. Res., Off. of Sci., U.S. Dep. of Energy, Washington, D.C.

Del Genio, A.D. and M.-S. Yao, 1993: Efficient cumulus parameterization for long-term climate studies: The GISS scheme. *The Representation of Cumulus*

Convection in Numerical Models, AMS Meteorol. Monogr., vol. 46, edited by K.A. Emanueal and D.A. Raymond, pp. 181-184, Am. Meteorol Soc., Washington, D.C.

Del Genio, A.D., M.-S. Yao, W. Kovari, and K.K. Lo, 1996: A prognostic cloud water parameterization for general circulation models. *J. Climate*, **9**, 270-304.

Del Genio, A.D., M.-S. Yao, and J. Jonas, 2007: Will moist convection be stronger in a warmer climate? *Geophys. Res. Lett.*, **34**, L16703, doi: 10.1029/2007/GL030525.

Delworth, T.L., et al., 2006: GFDL's CM2 global coupled climate models. Part I: Formulation and simulation characteristics. *J. Climate*, **19**, 643-674.

Diffenbaugh, N.S., and F. Giorgi, 2012: Climate change hotspots in the CMIP5 global climate model ensemble. *Climate Change*, **114(3-4)**, 813-822.

Donner, L.J., 1993: A cumulus parameterization including mass fluxes, vertical momentum dynamics, and mesoscale effects. *J. Atmos. Sci.*, **50**, 889-906.

Donner L.J., C.J. Seman, R.S. Hemler, and S. Fan, 2001: A cumulus parameterization including mass fluxes, convective vertical velocities, and mesoscale effects: Thermodynamic and hydrological aspects in a general circulation model. *J. Climate*, **14**, 3444-3463.

Donner, Leo J., Bruce Wyman, Richard S Hemler, Larry W Horowitz, Yi Ming, Ming Zhao, J-C Golaz, Paul Ginoux, Shian-Jiann Lin, M Daniel Schwarzkopf, John Austin, G Alaka, W F Cooke, Thomas L Delworth, Stuart Freidenreich,

C Tony Gordon, Stephen M Griffies, Isaac M Held, William J Hurlin, Stephen A Klein, Thomas R Knutson, Amy R Langenhorst, H C Lee, Y Lin, B I Magi, Sergey Malyshev, P C D Milly, Vaishali Naik, Mary Jo Nath, R Pincus, Jeff J Ploshay, V Ramaswamy, Charles J Seman, Elena Shevliakova, Joseph J Sirutis, William F Stern, Ronald J Stouffer, R John Wilson, Michael Winton, Andrew T Wittenberg, and Fanrong Zeng, July 2011: The dynamical core, physical parameterizations, and basic simulation characteristics of the atmospheric component AM3 of the GFDL Global Coupled Model CM3. *J. Climate*, **24(13)**, doi:10.1175/2011JCLI3955.1.

Druyan, L.M., 1991: The sensitivity of Sub-Saharan precipitation to Atlantic SST. *Climate Change*, **18**, 17-36.

Dunn, M, K. Johnson, and M. Jensen, 2011: The microbase value-added product: a baseline retrieval of cloud microphysical properties. U.S. Department of Energy. DOE/SC-ARM/TR-095.

Eldridge, R.H., 1957: A synoptic study of West African disturbance lines. *Quart. J. Roy. Meteor. Soc.*, **83**, 303-314.

Emanuel, K., 1994: "Atmospheric Convection". Oxford University Press, New York, 580 pp.

Han, Y. and E. R. Westwater, 2003: Analysis and improvement of tipping calibration for ground-based microwave radiometers. *IEEE Transactions on Geoscience and Remote Sensing*, **GRS-38**, 1260-1277.

Flato, G., J. Marotzke, B. Abiodun, P. Braconnot, S.C. Chou, W. Collins, P. Cox, F. Driouech, S. Emori, V. Eyring, C. Forest, P. Gleckler, E. Guilyardi, C. Jakob, V. Kattsov, C. Reason and M. Rummukainen, 2013: Evaluation of Climate Models. In: Climate Change 2013: The Physical Science Basis. Contribution of Working Group I to the Fifth Assessment Report of the Intergovernmental Panel on Climate Change [Stocker, T.F., D. Qin, G.-K. Plattner, M. Tignor, S.K. Allen, J. Boschung, A. Nauels, Y. Xia, V. Bex and P.M. Midgley (eds.)]. Cambridge University Press, Cambridge, United Kingdom and New York, NY, USA.

Fontaine B, Roucou P, Monerie P-A. 2011. Changes in the African monsoon region at medium-term time horizon using 12 AR4 coupled models under the A1b emissions scenario. *Atmospheric Science Letters*, **12**, 83–88, DOI: 10.1002/asl.321.

Frisch, A.S., C. W. Fairall, and J. B. Snider, 1995: Measurements of stratus cloud and drizzle parameters in ASTEX with a Ka-Band Doppler radar and a microwave radiometer. *J. Atmos. Sci.*, **52**, 2788-2799.

Garnache, R. R. and J. Fisher, 2003: Half-widths of H216O, H218O, H217O, HD16O, and D216O: I. Comparison between isotopomers. *J. Quant. Spectrosc. Radiat. Transfer*, **78**, 289-304.

GFDL Global Atmospheric Model Development Team, 2004: The new GFDL global atmosphere and land model AM2/LM2: Evaluation with prescribed SST simulations. *J. Climate*, **17**, 4641-4673.

Grabowski, W., 2001: Coupling cloud processes with the large-scale dynamics using the cloud-resolving convection parameterization (CRCP). *J. Atmos. Sci*, **58**, 978-997.

Güldner, J. and D. Spänkuch, 2001: Remote sensing of the thermodynamic state of the atmospheric boundary layer by ground-based microwave radiometry. *J. Atmos. Oceanic Technol.*,**18**, 925-933.

Harries, J.E., and Coauthors, 2005: The Geostationary Earth Radiation Budget project. *Bull. Amer. Meteorol. Soc.*, **86**, 945-960.

Ianova, D.D., L. Mitchell, W. P. Arnott, and M. Poellot, 2001: A GCM parameterization for bimodal size spectra and ice mass removal rates in mid-latitude cirrus clouds. *Atmos. Res.*, 59, 89-113.

Ilesanmi, O.O., 1971: An empirical formulation of an ITD rainfall model for the tropics: A case study of Nigeria. *J. Appl. Meeor.*, **10**, 882-891.

Illingworth, A., and S. Bony, 2009: Observational Strategies at Meso- and Large Scales to Reduce Critical Uncertainties in Future Cloud Changes. *Clouds in the Perturbed Climate System*, J. Heintzenberg and R.J. Charlson, Eds., MIT Press, 511-530.

IPCC, 2013: Summary for Policymakers. In: Climate Change 2013: The Physical Science Basis. Contribution of Working Group I to the Fifth Assessment Report

of the Intergovernmental Panel on Climate Change [Stocker, T.F., D. Qin, G.-K. Plattner, M. Tignor, S. K. Allen, J. Boschung, A. Nauels, Y. Xia, V. Bex and P.M. Midgley (eds.)]. Cambridge University Press, Cambridge, United Kingdom and New York, NY, USA.

Jakob, Christian, 2010: Accelerating Progress in Global Atmospheric Model Development through Improved Parameterizations: Challenges, Opportunities, and Strategies. *Bull. Amer. Meteor. Soc.*, **91**, 869–875.

Kim, D., A. Del Genio, and M.-S. Yao, 2011: Moist convection scheme in ModelE2. Technical report, NASA Goddard Inst. for Space Stud. arXiv:1312.7496.

Kim, D., H. Sobel, A.D. Del Genio, Y.-H. Chen S.J. Camargo, M.S. Yao, M. Kelley, and L. Nazarenko, The tropical subseasonal variability simulated in the NASA GISS general circulation model. *J. Climate.*, **25**, 4641-4659, doi: 10.1175/JCLI-D-11-00447.1.

Knupp, K. R., R. Ware, D. Cimini, F. Vandenberghe, J. Vivekanandan, E. Westwater, T. Coleman, and D. Phillips, 2009: Ground-based passive microwave profiling during dynamic weather conditions. *J. Atmos. Oceanic Tech.*, **26**, 1057-1073, doi: 10.1175/2008JTECHA1150.1

Kollias, P., M. A. Miller, K. L. Johnson, M. P. Jensen, and D. Troyan, 2009: Cloud, thermodynamic, and precipitation observations in West Africa during 2006. *J. Geophys. Res.*, **114**, D00E08, doi:10.1029/2008JD010641.

Lélé, M.I., and P.J. Lamb, 2010: Variability of the Intertropical Front (ITF) and rainfall over the West African Sudan-Sahel Zone. *J. Climate.*, **23**, 3984 – 4004.

Liao, L. and K. Sassen, 1994: Investigation of relationships between Ka-Band radar reflectivity and ice and liquid water contents. *Atmos. Res.*, **34**, 231-248.

Liljegren, J. C., B. M. Lesht, S. Kato, and E. Clothiaux, 2001a: Initial evaluation of profiles of temperature, water vapor, and cloud liquid water from a new microwave profiling radiometer. Proc. 11th Symposium on Meteorological Observations and Instrumentation, Albuquerque, NM, Amer. Meteor. Soc., 8.6.

Liljegren, J. C., B. Lesht, S. Kato, and. E. Clothiax, 2001b: "Initial evaluation of profiles of temperature, water vapor, and cloud liquid water from a new microwave profiling radiometer", presented at the 11th Atmospheric Radiation Measurement (ARM) Program Science Team Meeting, Atlanta, GA, 19-23 March 2001.

Liljegren, J. C., S. Boukabara, K. Cady-Pereira, and S. A. Clough, 2005: The effect of the half-width of the 22-GHz water vapor line on retrievals of temperature and water vapor profiles with a 12-channel microwave radiometer. *IEEE Transactions on Geoscience and Remote Sensing*, **43**, 1102 - 1108.

Liu, C. L. and A. J. Illingworth, 2000: Toward more accurate retrievals of ice water content from radar measurements of clouds. *J. Applied. Meteorol.*,**39**, 1130-1146.

Martin, G.M., M.A. Ringer, V.D. Pope, A. Jones, C.Dearden, and T.J. Hinton, 2006: The physical properties of the atmosphere in the new Hadley Centre Global Environmental Model, HadGEM1. Part I: Model description and global climatology. *J. Climate*, **19**, 1274-1301.

Mather, J.H., and J.W. Voyles, 2013: The ARM climate research facility: A review of structure and capabilities. *Bull. Am. Meteorol. Soc.* **94**, 377 – 392.

Meehl, G.A., C. Covey, T. Delworth, M. Latif, B. McAvaney, J.F.B. Mitchell, R.J. Stouffer, and K.E. Taylor, 2007: The WCRP CMIP3 multi-model dataset: A new era in climate change research. *Bull. Amer. Meteor. Soc.*, **88**, 1383-1394.

Miller, M., V. Ghate, and R. Zahn, 2012: The radiation budget of the West African Sahel and its controls: A perspective from observations and global climate models. *J. Climate*. **25**, 5976-5996, doi:10.1175/JCLI-D-11-00072.1.

Miller, R. L., A. Slingo, J.C. Barnard, and E. Kassianov, 2009: Seasonal contrast in the surface energy balance of the Sahel. *J. Geophys. Res.*, **114**, D00E05.

Miller, M. A., and A. Slingo, 2007: The ARM Mobile Facility and its first international deployment: Measuring radiative flux divergence in West Africa. Bull. Amer. Meteor. Soc., 88, 1229-1244, doi: 10.1175/BAMS-88-8-1229.

Monkam, D., 2002: Convective available potential energy (CAPE) in northern Africa and tropical Atlantic: A study of it connections with rainfall in central and west Africa during summer 1985. *Atmos. Res.*, **62**, 125-147.

Mlawer, E. J., S. A. Clough, and D. C. Tobin, 2003: "The MT_CKD water vapor continuum: A revised perspective including collision induced effects", presented at the Atmospheric Science from Space using Fourier Transform Spectroscopy (ASSFTS) Workshop, Bad Wildbad (Black Forest), Germany, 8-10 October 2003.

Mora, C.F., A.G., R.J. Longman, R.S. Dacks, M.M. Walton, E.J. Tong, J.J. Sanchez, L.R. Kiaser, Y.O. Stender, J.M. Anderson, C.M. Ambrosino, I. Fernandez-Silva, L.M. Gluseffi, and T.W. Giambelluca, 2013: The projected timing of climate departure from recent variability. *Nature*, **502**, 183-187.

Niang, I., O.C. Ruppel, M.A. Abdrabo, A. Essel, C. Lennard, J. Padgham, and P. Urquhart, 2014: Africa. In: Climate Change 2014: Impacts, Adaptation, and Vulnerability. Part B: Regional Aspects. Contribution of Working Group II to the Fifth Assessment Report of the Intergovernmental Panel on Climate Change [Barros, V.R., C.B. Field, D.J. Dokken, M.D. Mastrandrea, K.J. Mach, T.E. Bilir, M. Chatterjee, K.L. Ebi, Y.O. Estrada, R.C. Genova, B. Girma, E.S. Kissel, A.N. Levy, S. MacCracken, P.R. Mastrandrea, and L.L. White (eds.)]. Cambridge University Press, Cambridge, United Kingdom and New York, NY, USA, pp. 1199-1265.

Randall, D.A., M. Khairoutdinov, A. Araawa, and W. Grabowski, 2003: Breaking the cloud parameterization deadlock. *Bull. Amer. Meteor. Soc.*, **84**, 1547-1564.

Randall, D.A, R.A. Wood, S. Bony, R. Colman, T. Fichefet, J. Fyfe, V. Kattsov, A. Pitman, J. Shukla, J. Srinivasan, R.J. Stouffer, A. Sumi and K.E. Taylor, 2007: Climate Models and Their Evaluation. In: Climate Change 2007: The Physical Science Basis. Contribution of Working Group I to the Fourth Assessment Report of the Intergovernmental Panel on Climate Change [Solomon, S., D. Qin, M. Manning, Z. Chen, M. Marquis, K.B. Averyt, M. Tignor and H.L. Miller (eds.)]. Cambridge University Press, Cambridge, United Kingdom and New York, NY, USA

Revercomb, H. and Coauthors, 2003: The ARM program's water vapor intensive observation periods. *Bull. Am. Meteor. Soc.* **84**, 217 – 236.

Roehrig, R., D. Bouniol, F. Guichard, F. Hourdin, and J.-L. Redelsperger, 2013: The present and future of the West African monsoon: A process-oriented assessment of CMIP5 simulations along the AMMA transect. *J. Climate*, **26**, 6471 – 6505, doi: 10.1175/JCLI-D-12-00505.1.

Rosenkranz, P., 1998: Water vapor continuum absorption: A comparison of measurements and models. *Radio Sci.*, **33**, 919-928.

Russell, G.L., J.R. Miller, and D. Rind, 1995: A coupled atmosphere-ocean model for transient climate change studies. *Atm.-Ocean*, **33(4)**, 683-730.

Satoh, M., T. Matsuno, and H. Tomita et al., 2008: Nonhydrostatic icosaherdral atmospheric model (NICAM) for global cloud-resolving simulations. *J. Comp. Phys.*, **227**, 3486-3514.

Schmetz, J., P. Pili, S. Tjemkes, D. Just, J. Kerkmann, S. Rota, and A. Ratier, 2002: An introduction to Meteosat Second Generation (MSG). *Bull. Amer. Meteor. Soc.*, 83, 977-992.

Schmidt et al., 2006: Present-day atmospheric simulations using GISS ModelE: Comparison to in situ, satellite, and reanalysis data. *J. Climate*, **19**, 153-192

Schmidt G.A., et al., 2014: Configuration and assessment of the GISS ModelE2 contributions to the CMIP5 archive. *J. Adv. Model. Earth Syst.*, **6**, 141-184, doi: 10.1002/2013MS000265.

Schroeder, J. A. and E. R. Westwater, 1991: "Users Guide to WPL Microwave Radiative Transfer Software," Report ERL-WPL-213, NOAA Environmental Research Laboratory, Boulder, CO.

Settle, J.J., N.A. Bharmal, G.J. Robinson, and A. Slingo, 2008: Sampling uncertainties in surface radiation budget calculations in RADAGAST. *J. Geophys. Res.*, **113**, D00E02, doi: 10.1029/2008JD010509.

Siebesma, A.P., and Coauthors, 2009: Cloud-controlling Factors. Clouds in the Perturbed Climate System, J. Heintzenberg and R.J. Charlson, Eds., MIT Press, 269-290.

Slingo, A., et al., 2008: Overview of observations from the RADAGAST experiment in Niamey, Niger: 1. Meteorological and thermodynamic variables. *J. Geophys. Res.*, **113**, D00E01, doi: 10.1029/2008JD009909.

Slingo, A., H.E. White, N.A. Bharmal, and G.J. Robinson, 2009: Overview of observations from the RADAGAST experiment in Niamey, Niger: 2. Radiative fluxes and divergences. *J. Geophys. Res.*, **114**, D00E04, doi: 10.1029/2008JD010497.

Solheim F., J. Godwin, and R. Ware, 1998a: Passive ground-based remote sensing of atmospheric temperature, water vapor, and cloud liquid water profiles by a frequency synthesized microwave radiometer. *Meterologische Zeitschrift, N. F.*, **7**, 370-376.

Solheim, F., J. R. Godwin, E. R. Westwater, Y. Han, S. J. Keihm. K. Marsh, and R. Ware, 1998b: Radiometric profiling of temperature, water vapor and cloud liquid water using various inversion methods. *Radio Sci.*, **33**, 393-404.

Stackpole, J. D., 1967: Numerical analysis of atmospheric soundings. *J. Appl. Meteor.*, **24**, 640-657.

Stephens, G.L., 2005: Cloud feedbacks in the climate system: a critical review. *J. Climate*, **17**, 3661-3665.

Stoffel, T., 2005: Solar Infrared Radiation Station (SIRS) handbook. ARM TR-025. Department of Energy, Washington DC, 29 pp. [Available online at http://www.arm.gov]

Trabachino, L. and M.A. Miller, 2014: Thermodynamic profiling capabilities of the microwave radiometer profiler in various locations of interest for atmospheric model development. In Atmospheric System Research Science Team Meeting, 10-14 March 2014, Potomac, MD.

Troyan, D., 2012: Merged Sounding Value-Added Product Technical Report. U.S. Department of Energy. DOE/SC-ARM-TR-102.

Ware, R., R. Carpenter, J. Güldner, J. Liljegren, T. Nehrkorn, F. Solheim, and F. Vandenberghe, 2003: A multichannel radiometer profiler of temperature, humidity, and cloud liquid. *Radio Sci.*, **38**, 8079, doi:10.1029/2002RS002856.

Westwater, E. R., Y Han, and F. Solheim, 2000: Resolution and accuracy of a multi-frequency scanning radiometer for temperature profiling. Microw. Radiomet. Remote Sens. Earth's Surf. Atmosphere, P. Pampaloni and S. Paloscia (Eds.), pp. 129-135.

Wilcox E.M., and L.J. Donner, 2007: The frequency of extreme rain events in satellite rain-rate estimates and an atmospheric general circulation model. *J. Climate*, **20**, 53-69.

Williams, K.D., and G. Tselioudis, 2007: GCM intercomparisons of global cloud regimes: Present-day evaluation and climate change response. *Climate Dyn.*, **20**, 231-250.

Williams, K.D. and M.J. Webb, 2008: A quantitative performance assessment of cloud regimes in climate models. *Clim. Dyn.*, **33**, 141-157.